DYNAMIC MAGNETIC X-POINTS

J.N. Leboeuf[†], T. Tajima,
and J.M. Dawson[†]

March 1981

[†] Department of Physics
University of California
Los Angeles, California 90024

J. N. Leboeuf
Department of Physics
University of California
Los Angeles, California 90024

T. Tajima
Institute for Fusion Studies
University of Texas
Austin, Texas 78712

J. M. Dawson
Department of Physics
University of California
Los Angeles, California 90024

ABSTRACT

Two-and-one-half dimensional magnetostatic and electromagnetic particle simulations of time-varying magnetic x-points and the associated plasma response are reported. The stability and topology depend on the crossing angle of the field lines at the x-point, irrespective of the plasma β. The electrostatic field and finite Larmor radius effects play an important role in current penetration and shaping of the plasma flow. The snapping of the field lines, and dragging of the plasma into, and confinement of the plasma at, an o-point (magnetic island) is observed. Magnetic island coalescence with explosive growth of the coalescence mode occurs and is accompanied by a large increase of kinetic energy and temperature as well as the formation of hot tails on the distribution functions.

I. Introduction

Tearing instabilities are believed to play an important role in a wide variety of physical phenomena ranging from solar flares[1] to reconnection in the magnetosphere[2] and to magnetic fluctuations and island formation in tokamak discharges.[3]

Earlier linear[4,5] and nonlinear theories[6] of the tearing mode were largely based on collisional magnetohydrodynamics (MHD) equations. It was however recognized that the collisional description might not be adequate for space plasmas and for the higher temperature fusion discharges where mean free paths are large compared to the spatial dimensions involved. Collisionless descriptions of the linear tearing mode[7,8] were then attempted which culminated in the fully kinetic treatment of both the linear and nonlinear evolutions of tearing modes by Drake and Lee.[9,10]

Experimentally, research on tearing modes in tokamaks is limited by diagnostic difficulties, e.g., internal magnetic field topologies are inferred from external measurements or indirectly from x-ray data.[11,12] Observations of reconnection phenomena in space from satellites[13] present the most direct measurements but from a single spacecraft passing through a reconnection region, the three-dimensional time-dependent picture cannot be mapped. Many laboratory experiments on magnetic field line reconnection[14,15,16] have been performed in pinches, which are difficult to diagnose internally with good space and time resolution. However, sophisticated experiments have recently been carried out at UCLA[17] in a large plasma device where an x-point magnetic field is created by external current sheets. Detailed information on reproducible reconnection events involving time and space resolved measurements of both the magnetic field topology and plasma parameters in three-dimensions have been obtained.[18]

Nonlinear MHD simulations of the resisitive tearing mode were first carried out by Cross and Van Hoven.[19] Subsequently, Rosenbluth and his co-workers[20]

studied the nonlinear evolution of resistive kink and tearing modes in tokamaks. Since then, MHD simulations of tearing modes have been actively pursued in attempts at modelling disruptions in tokamak discharges. Such a disruptive instability has been attributed to the growth of one tearing mode[21]; to the coupling of many modes[22,23]; and to the interaction of a tearing mode with the walls.[24] Following the theoretical work of Finn and Kaw,[25] MHD simulations of island coalescence starting from an equilibrium chain of magnetic islands[26] have verified that these island chains are unstable to coalescence but no threshold with island width was found in the simulations as contrasted with the theory. The results of these simulations were subsequently verified with a finer computational mesh[27]. With applications to geomagnetic substorms in mind, Sato and his coworkers[28] carried out MHD simulations of flow-driven reconnection by forcing a flow of plasma into an x-point. The forced reconnection of the x-point field lines resulted in a conversion of magnetic energy to kinetic energy. Fast magnetospheric particles thus produced would then stream down the field lines, reach the ionosphere and produce the auroras. All of these MHD simulations represent studies of resistive tearing modes.

Simulations of the collisionless tearing instability are best carried out with particle codes, which are designed to minimize collisions and to describe kinetic collective plasma effects. The codes used have all been magnetostatic, i.e., they solve the full set of Maxwell's equations neglecting the displacement current (a good approximation if low frequency electromagnetic phenomena are of interest). So doing, Dickman et. al.[29] observed magnetic island formation and coalescence in particle-in-cell simulations of axisymmetric finite-β plasma configurations. Drift-Alfven and double tearing instabilities have also been studied on a finite size particle code by A. T. Lin.[30] A detailed study with a similar code by Katanuma and Kamimura[31] found that electrostatic effects have a tendency to enhance the tearing mode growth rate. For multi-mode tearing, a combination of

magnetic islands was observed.

We report here simulations of magnetic field lines reconnection at an x-type neutral line carried out on magnetostatic and electromagnetic finite-size particle codes. These simulations are sufficiently collisionless (the magnetic Reynolds number S > 800) and include both electrons and ions dynamics, allowing for charge separation effects and finite Larmor radius effects. The set-up is roughly similar to the experimental one of Stenzel and Gekelman[17] but involves only a two dimensional model. In our periodic system, the x-point magnetic field is induced by two external current sheets in which the current rises in time. Compression of the plasma ensues which forces a flow through the x-point. The system size, magnetic field strength and plasma parameters can be varied and numerous diagnostics performed. The main features which emerge out of this investigation are as follows: i) the stability of the x-point geometry depends on the crossing angle θ of the field lines at the x-point, irrespective of the plasma β where β is the ratio of plasma pressure to magnetic pressure. It is unstable for narrow angles. ii) Charge separation and finite Larmor radius effects cause rapid initial current penetration and play an important role in shaping the plasma flow. iii) A large gain in kinetic energy and temperature and the formation of hot tails on the distribution functions occur only from magnetic islands coalescence following their formation by the tearing mode.

The organization of this paper is as follows. The models and initial conditions are described in Sec. II. The topological changes of the external x-point magnetic field and associated plasma behavior are presented in Sec. III. Sec. IV treats energy transfer and the heating of the particles. We summarize and discuss the results in Sec. V.

II. Models and Initial Conditions

Two different codes, one magnetostatic[32] and the other electromagnetic[33] have been used to simulate time-varying x-point geometries within the framework of finite-size particle simulations. For reasons of convenience, a relativistic version of the electromagnetic code is used. Both codes have two-and-one-half, three fields and velocities (x, y, and z) and two space (x, y), dimensions and are periodic in both the field and particle quantities. They include mobile ions with ion-to-electron mass and temperature ratios of $M_i/m_e = 10$ and $T_i/T_e = 1/2$, respectively. Here, for historical reasons, the electrons are positively charged and the ions negatively charged. Space charge fields, for instance, will then be the negatives of the usual ones. Both species of particles are given Maxwellian velocity (in the magnetostatic code) or momentum (in the electromagnetic code) distributions in all three directions at time t = 0. Four particles per unit square cell were used; all are loaded uniformly in space, so that the density is uniform at t = 0. The speed of light is fixed at $c = 5 v_{te}$, with v_{te} being the electron thermal velocity at t = 0, so that the collisionless skin depth $\delta = c/\omega_{pe} = 5 \lambda_e$, where ω_{pe} and λ_e are respectively the electron plasma frequency and the electron Debye length at t = 0. The system size is varied from $L_x \times L_y = 32\Delta \times 32\Delta$ to 64 x 32 and to 128 x 32, with the unit grid spacing Δ and the particle size equal to one electron Debye length at t = 0. One other case was run with $L_x \times L_y = 256\Delta \times 16\Delta$, with collisionless skin depth $c/\omega_{pe} = 3\Delta$ and a ratio of thermal velocity to the speed of light of $v_{te}/c = 1/6$ and otherwise identical parameters to the other system sizes.

The x-point geometry is established by external current sheets placed at y = 0 and $y = L_y$ which extend along x with a gap of length x_g from x = 0 to $x = x_g$ at the left end and $x = (L_x - x_g)$ to $x = L_x$ at the right end. The gap length is $x_g = 5\Delta$ for all system sizes other than 32 x 32 where it was taken

to be $x_g = 10\Delta$. The external or vacuum field is displayed in Fig. 1(a) for a 64 x 32 system. Periodicity, which requires closing of the field lines, induces the island at the edge, stably pinned in the gap between the sheets. The magnetic field is then linear between the plates as shown in Fig. 1(b). Without the gap, field lines running in opposite directions with a neutral line at the center of the system would be established instead of the x-point magnetic field geometry.

At t = 0 the current is zero in the sheets and the system is in thermal equilibrium. The current rises sinusoidally from zero at t = 0 up to a maximum at the quarter period after which it is kept constant (crow-bar phase). To prevent overshoot and insure a smooth plasma response, the rise time of the current in the sheets is chosen to be $\tau_r = 31.4 \, \omega_{pe}^{-1}$, greater than or equal to the magnetosonic transit time from center to the driving currents for all the plasma β's investigated. By varying the strength of the currents in the sheets, different plasma β's can be achieved. The plasma β is measured here as the ratio of the initial plasma kinetic energy density to the magnetic energy density, with the magnetic field evaluated at its maximum in space (at the sheets) and time (at crow-bar). There is no external component of the magnetic field (here in the ignorable z-direction) normal to the x-point field, i.e. if we were modeling a tokamak only a poloidal field would be present and there would be no toroidal field.

Because of the external driving currents a net external current, albeit spatially localized, is flowing through each period of the system. Unless there is a counter current, the system will not be periodic and there will be an infinite magnetic energy over the infinite doubly periodic system. Furthermore, if

there is a net current in the z-direction, there must be a net accumulation
of charge at z = ±∞. This would produce an electric field that will try to
generate a return current in the plasma which cancels out the net current.
We include this electric field in our treatment.

To do this, we retain the k = 0 component of the plasma and external
current densities as well as the k = 0 component of the electric field in
Ampere's law in the direction of the external current flow so that

$$\frac{\partial E^z \ (k = 0)}{\partial t} = -4\pi \ [J^z_{ext} \ (k = 0) + J^z_p \ (k = 0)] \tag{1}$$

where E is the transverse electric field, t the time, J_{ext} the external
current and J_p the plasma return current. This is rather trivial to
implement in the electromagnetic code but the magnetostatic code is complicated
somewhat by retaining the k = 0 component of the current because of the
iterative solution of Faraday's law.[32]

We have verified that this procedure yields physically reasonable results
that are almost identical when both electromagnetic and magnetostatic codes
are run against each other with the same parameters. That the return plasma
current does indeed compensate the external sheet current very closely is
shown in Fig. 1(c) where the space-integrated components of both currents
in the z direction (their k = 0 components), is displayed for a 64 x 32 system;
the currents are of equal magnitude but of opposite sign. Even though the
total plasma current is equal to the plate current, the current density
achieved by the plasma locally is usually smaller than the current density
at the sheets. We have encountered some numerical difficulties with the
magnetostatic code for low β plasmas where plasma compression is severe as
the current rises in the plates and a vacuum can even be formed, at which

point the Alfven speed becomes very large and the code exhibits instability[32]; in such cases we elected to use the electromagnetic code.

The magnetic Reynolds number of our configuration can be estimated as follows. Electron - ion collisions determine the resistivity. The collision frequency for our finite-size particles in two-dimensions is[34]

$$\nu_{ei}/\omega_{pe} = (\frac{1}{12}) \times (\frac{1}{16n\lambda_e^2}), \tag{2}$$

where the factor of 1/12 is the reduction factor due to the finite-size of the particles as compared to point particles collisions. Here, 4 particles are used per Debye square and $\nu_{ei} \sim (800)^{-1} \omega_{pe}$. The magnetic Reynolds number is defined as $S = 4\pi v L/\eta c^2$, where v is a typical velocity on the mesh, L a typical length scale and η is the resistivity expressed as $\eta = m\nu_{ei}/n_o e^2$ with e the electron charge, m the electron mass and n_o the average electron density. In terms of the simulation parameters, this yields

$$S = (\omega_{pe}^2/c^2) \, vL/\nu_{ei} = (L/\delta^2) \, (v/\nu_{ei}), \tag{3}$$

where δ is the collisionless skin depth. With $\delta = 5\lambda_e$, $L = 32\lambda_e$ and $v = v_A \sim v_{te}$ where v_A is the Alfven speed (both typical values for the simulations presented here), Eq. (3) gives $S \sim 800$. Resistance can also be supplied by wave-particle interactions such as Landau damping or wave trapping[7].

The above gives a minimum value for S because collisions between the particles in the x-y plane are not very effective in inhibiting the current flow. The current flows in the z-direction, which is the ignorable one here, and the

collisionality is much smaller in that direction than the in-plane one calculated above.

The modification to the external x-point geometry by the plasma response to the current rise in the sheets (which establishes the x-point geometry) is discussed next.

III. Topologies and Plasma Dynamics

The plasma dynamics resulting from various driving current geometries and plasma betas were investigated. The driving current rises in time to its peak value where it is crow-barred; the magnetic field rises along with it in the vicinity of the driving currents. The electrons respond quickly to the inductive field generating a current which attempts to shield out the magnetic field. The magnetic pressure or J x B force drives the electrons inward creating a charge separation; this creates an electrostatic field which balances the J x B force on the electrons and transfers the magnetic pressure force to the ions. The ions are driven inward. At the same time the magnetic field is strongly modified by the plasma currents altering the magnetic topologies. The resulting current sheet is subject to the collisionless tearing mode which results in the formation of magnetic islands (o-points). It is found that whether or not tearing takes place depends on the magnetic topology; when a 32 x 32 system was run on the magnetostatic code the field pattern was essentially that for the vacuum field (the field lines cross at 90°) for all cases tried and no instability was observed. However, for all cases run where the current sheet was longer than wide tearing occured. In all the investigations reported here the characteristic lengths such as the thickness of the current sheet or the dimensions of magnetic islands are only a few collisionless depths (typically 5).

III. A. A Stable Configuration

Here, we consider the case of a system size L_x x L_y = $32\lambda_e$ x $32\lambda_e$ with plasma parameters of β = 0.073, electron and Larmor radii of ρ_e = $0.78\lambda_e$ and ρ_i = $1.75\lambda_e$. The thermal velocities used are the initial ones and the magnetic fields are evaluated at the crow-bar time and at the plates so that ω_{ce} = $1.28\omega_{pe}$ and ω_{ci} = $0.128\omega_{pe}$. The Alfven speed calculated for the same value of the

magnetic field and average density is $v_A = 2v_{te}$. The Alfven frequency at the fundamental mode is $\omega_A \simeq 0.4\omega_{pe}$ and the Alfven time $\tau_A = 15.8\omega_{pe}^{-1}$. The run extends up to $\omega_{pe}t = 200$ or 13 Alfven times.

The field lines at various times in the run are displayed in Fig. 2; these are contours of the z-component of the vector potential. Once the external x-point configuration is established at full magnetic field strength, there are no further changes in topology. The edge island is stably pinned in the gap between the sheets and the plasma magnetic field is close to the vacuum field. The plasma does not sit idle during this, however. Fig. 3 where the ion density and current density are displayed shows early compression of the plasma resulting in the encounter of two plasma masses at the x-point at crow-bar. There is, however, no evidence for neutral sheet formation. After crow-bar, the particle density and current density are higher at the o-point and preserve the magnetic configuration. The mass flow and electrostatic field plotted in Fig. 4 show flow into the x-point during compression or rise of the current in the plates and an electric field directed away from the center towards the plates pulling the ions towards the x-point. The J x B force has the same effect. The mass flow is then away from the x- but into the o-point where the J x B force and the electrostatic field act to confine the ions. Late in the run, the mass flow is quite random within the o-point. The flow patterns before and slightly after crow bar are similar to the ones observed by Sato et al.[28] in their MHD simulations. Flow induced reconnection with magnetic energy transfer to the particles was observed there. Here, while there is still some energy fed in by the driving currents, no modification of the topology takes place after crow-bar.

Various runs with plasma β's up to 5 also showed that no modification of the topology occurred although the plasma response was more turbulent (not as coherent). Electromagnetic runs for the same set-up and parameters reproduce these results. For these cases the field lines cross at 90° and the magnetic tension appears to be sufficient to hold the original configuration. This behavior may be attributed to the fact that in the present simulations the magnetic island scalelength or the x-point scalelength is only several times the electron collisionless skin depth. This means that the magnetic flux can penetrate more or less freely to the x-point with the penetration enhanced by collisionless dissipation (anomalous skin depth). On the other hand, in the MHD picture, the collisionless skin depth is zero and it is much more difficult for the flux to go through the x-point.

Another departure from the MHD picture is that an electrostatic field is established which points from center to the plates; it means an excess of electrons exists in the center. This is accomplished because the electrons are pushed inward first and charge separation, with the ions left behind, ensues.

Naively, one might expect the electrons to have the smaller excursion because of their smaller Larmor radius. However, because of their low mass the electrons closely follow the motion given by $E + v/c \times B = 0$. As the z-current runs in the plates and an induced electric field is established in that direction so that electrons move in the y-direction in accordance with $v_y = \pm |E_z| / |\beta_x|$ and the electrons move towards the center frop top (-) and bottom (+). The ions do not follow because of their larger inertia. This electron excursion leads to an electrostatic field pointing from center to plates which pulls the (negatively charged) ions in towards the x-point. The return plasma current in the z-direction is primarily carried by the electrons experiencing $E_y \times B_x$ drifts. Initially at least, the return plasma current is maximum close to the plates and not where the

density is higher. Normally E x B drifts do not produce a current for electrons and ions because both drift in the same direction. However, it takes a cyclotron period for the ions to pick up this drift and so they do not follow; also they pass through the current sheath because of their large orbits before they acquire the E x B velocity[35].

The different response of the electrons and the ions is illustrated by the orbit plots of Fig. 5. We have plotted as a point the position (x, y) of an electron at the o-point at crow bar and at the x-point at crow-bar at different times in the run. The same procedure is adopted for x-point and o-point ions. In spite of their smaller Larmor radius, the electrons travel throughout the whole plane. On the other hand, the ions with quite large a Larmor radius eventually end up at the o-point where they remain confined electrostatically.

III. B. High β Unstable Configuration and Low β Field Line Snapping

As already stated interesting behavior was obtained only for systems which were longer than they were thick. Here we consider the case of a 64 x 32 system where the angle of the x-point is 53° for the vacuum condition. For the plasma pressure and external current used here, the plasma β is 5. Other parameters for this run are $\rho_e = 6.5\lambda_e$, $\rho_i = 14.5\lambda_e$ and $\omega_{ce} = 0.16\omega_{pe}$, whereas $\omega_{ci} = 0.016\omega_{pe}$. The Alfven velocity is calculated to be $v_A = 0.24v_{te}$, so that the Alfven time for the fundamental mode is $\tau_A = 266\omega_{pe}^{-1}$. The run in this case only extends to cover one Alfven time or about two sonic times. All parameters are again those for maximum magnetic field strength (at crow-bar and at the plates), average density and initial temperatures. This 64 x 32 run shows that for this 2 to 1 system with large plasma β, the plasma can substantially modify the x-point magnetic field geometry. This is shown in Fig. 6

where the magnetic field lines are displayed at various times in the run and compared to the external magnetic x-point geometry. Noteworthy features are the displacement of the x-point along the x-axis (associated with the growth of the externally produced island in the gap) during the rise time of the field (up to $\omega_{pe}t = 31.4$), and the appearance of an elongated island after crow-bar (see the time $\omega_{pe}t = 40$ in Fig. 6), with the width of the current channel of the order of 2 collisionless skin depths ($\delta = c/\omega_{pe} = 5\lambda_e$). The broad current channel then breaks up to yield an island at the position of the original x-point ($\omega_{pe}t = 80$ in Fig. 6) which then attaches and detaches repeatedly to and from the island in the gap between the sheets. For this high β case, the plasma response is turbulent. The electrostatic field still appears to shape the incoherent mass flow; the $J \times B$ force is weak but coherently points towards the x-point. Little density compression is observed (a factor of 1.2 at crow-bar as expected) as the current rises in the sheets. As we shall see later, there is inconsequential heating of the particles and negligible energy transfer between fields and particles, because there is little available magnetic energy to start with in the x-point. While plasma induced modifications of the vacuum x-point geometry do occur in this longer than thick high β case, these are more likely due to nonequilibrium turbulence generated by the driving fields than to an instability.

For these high β's, the behavior of the x-point depends on the crossing angle of the field lines θ or on the ratio of the magnetic field scalelengths in both directions: $\theta = \tan^{-1}(\lambda_y/\lambda_x)$ where λ_y is the fundamental wavelength of characteristic magnetic field variation in the y-direction and λ_x the same quantity in the x-direction, approximately $L_y/2$ and $L_x/2$ here. The fact that only one island is obtained for $L_x = L_y$ but two islands form for $L_x = 2L_y$

suggests the following scaling for the number of islands N:

$$N \simeq L_x/L_y. \tag{4}$$

This scaling may also include a dependence on β. For a 256 x 16 system with $\beta \sim 0.07$, for example, the neutral sheet does initially tear into 16 islands, as we will present in Sec. III C.

First attempts at lowering the plasma β in a 64 x 32 unstable system were in the magnetostatic code. For $\beta = 1$, for example, a neutral sheet was clearly formed and a magnetic island appeared at the position of the external x-point. Substantial compression followed with a coherent flow first into the x-point up to crow bar and then out of the x-point into the o-point where the particles accumulated. Without altering the algorithm further or drastically reducing the time-step to accommodate compression[32], the code became numerically unstable. On the basis that a vacuum could be formed, the magnetostatic code was replaced by the electromagnetic code thereafter for the low β cases presented here. These electromagnetic runs show that lowering the plasma β for the same system size produces a more coherent plasma behavior and major modifications to the x-point magnetic field topology result.

We now present the case for $\beta = 0.2$. Other parameters are electron and ion Larmor radii of 1.3 λ_e and 2.94 λ_e. The electron and ion gyrofrequencies are $\omega_{ce} = 0.76\ \omega_{pe}$ and $\omega_{ci} = 0.076\ \omega_{pe}$. The Alfven time for the fundamental wavelength in the x-direction is 60.7 ω_{pe}^{-1}, with an Alfven speed $v_A \simeq v_{te}$. This is a magnetized case.

The magnetic field lines are displayed in Fig. 7 and compared to the external x-point magnetic field configuration. Within the rise time of

the current, a thin neutral sheet is formed. The horizontal field lines

flatten near the neutral region, as predicted by the classical pictures of

merging[5] and observed experimentally[17]. The original x-point configuration

turns into a stretched field line configuration with two y-points ($\omega_{pe}t = 30$ in

Fig. 7). The ion density contours of Fig. 8, where the dotted contours refer

to a density below the average one at a particular instant and the full ones

to a density above the instantaneous average, reveal a high density region

(3 times the initial density) at the center of the system, with a vacuum

forming close to the plates when the two y-points magnetic field configuration

is established. The width of the neutral sheet region $\Delta y = 4\lambda_e$ corresponds to

the collisionless skin depth evaluated using the local plasma frequency so that

$c/1.7 \, \omega_{pe} \sim 3 \, \lambda_e$. The plasma current density is also displayed in Fig. 8

at equivalent times. Dotted contours indicate regions of high plasma return

current. The current channel at $\omega_{pe}t = 30$ is broad with a width $\Delta y \simeq 16 \, \lambda_e$ and

runs along the neutral line with a length $\Delta x \simeq 40\lambda_e$. This neutral sheet config-

uration is maintained for about one Alfven time, at which point the topology

reverts back to one with the x-point at the center of the system ($\omega_{pe}t = 90$ in

Fig. 7), and the density maximum (2.5 times the initial density) is located at

the island stably pinned in the gap between the sheets. The current channel

is especially narrow at the x-point location with a width $\Delta y = 8\lambda_e$. Again,

one Alfven time later, all the particles end up in the island in the gap and

a vacuum is formed in the center of the system ($\omega_{pe}t = 150$ in the ion density

plot of Fig. 8). As seen in Fig. 8, the plasma current is concentrated at

the o-point. The magnetic field topology displayed in Fig. 7 now consists of

a large island in the gap and an x-point residing in vacuum at the center of

the system. The magnetic topology, the ion density, and the current do not

change from then on until the end of the run at $\omega_{pe}t = 300$.

This change in magnetic topology is analogous to the stretching of a rubber-band (here the field lines) held fixed at two points (here the gaps) and sudden snapping of this rubberband (by field line reconnection). Snapping of the field lines drags plasma into the o-point. As we shall see in the next section, we now observe substantial net increase of the particle energy over the crow-bar level during this process for the first time. The energies then oscillate about the value achieved at $\omega_{pe}t = 150$ until the end of the run.

We display in Fig. 9 the electrostatic field and the mass flow. During the rise time of the current, the flow is forced into the x-point ($\omega_{pe}t = 30$). This is accompanied by an electric field which points from the x-point to the plates and forces the ions into the x-point. Later on in time, the mass flow is from the x-point into the o-point, where the plasma remains confined. From $\omega_{pe}t = 150$ on, the flow at the o-point is incoherrent. The effect of the electrostatic field is the confine the ions at the o-point. This is clear from the particle orbits presented in Fig. 10. Ions originally at the x-point and o-point regions end up at the island in the gap. Electrons originally at the x-point and o-point regions spend more time at the o-point but wander through the whole area. On the other hand, the ions with essentially infinite Larmor radius are confined at the o-point.

C. Magnetic Island Coalescence

In order to explore cases where larger transfer of energy to the particles takes place during the snapping process, a longer system in the x-direction was set up ($L_x = 128\lambda_e$: double the snapping size). Snapping did not occur in the same way in this run; an island was formed in the place of the original x-point and coalescence with the island in the gap happened.

The system size for this run is $L_x \times L_y = 128\lambda_e \times 32\lambda_e$. The current in the sheets is such that $\beta = 0.2$, as before, and the electrons and ion Larmor radii are $\rho_e = 1.3\lambda_e$ and $\rho_i = 2.9\lambda_e$ while the gyrofrequencies are $\omega_{ce} = 0.77\omega_{pe}$ and $\omega_{ci} = 0.077\omega_{pe}$. The alfven velocity is $v_A = 1.22\ v_{te}$ so that the Alfven time for the fundamental wavelength in the x-direction is $\tau_A \simeq 105\ \omega_{pe}^{-1}$. The crossing angle of the field lines is $\theta \simeq 28°$.

The magnetic field topology is plotted in Fig. 11 at various times of the run and compared with the external x-point magnetic field. The ion density and plasma current are displayed in Fig. 12. A neutral sheet is established within the rise time of the current. The neutral sheet tears and forms an island in the middle of the system at the place of the original x-point within an Alfven time. The island width to length ratio is $\Delta_y/\Delta_x = 4/50$ at $\omega_{pe}t = 50$; it is again one collisionless skin depth wide. Substantial pile-up of the density and current at the center island occurs and this island swells, as does the island in the gap where a simular density concentration happens. The islands width to length ratio is $\Delta_y/\Delta_x = 30/60$ at $\omega_{pe}t = 150$. Vacuum appears outside the islands. The particle density (5 times the initial one) and plasma current density in both islands are comparable. Past this saturated island growth state, attraction of the current filaments induces displacement of the island at the center towards the one in the gaps. The attraction force of the adjacent current has overcome the stabilizing one arising from the squeezing of flux surfaces up against the x-points. Coalescence is complete at $\omega_{pe}t = 150$. The peak density is about 6 times the original density, and the return plasma current density concentrated at the coalesced island exceeds the sheet current density. Vacuum prevails outside of the coalesced island. Till the end of the run at $\omega_{pe}t = 400$, the coalesced island in the

gap remains entrapped there and repeatedly expands to an oblate shape and contracts to a more cylindrical one. Both the $J \times B$ force and the electrostatic field combine to force the flow first into the x-point as the center island is formed where part of the plasma is trapped, then from the x-point region into the o-point in the gap as both center island and edge island swell; both tend to confine the plasma at the o-points. The mass flows are turbulent inside the islands in the saturated islands phase. During coalescence, the flows inside the two magnetic islands are about of equal magnitude but point against each other. In the merged state, the mass flow is again turbulent inside the island and the plasma gains heat by collisions and turbulent dissipation.

The kinetic energy increase achieved by coalescence is an order of magnitude above the energy increase gained by compression during the island formation phase. Heating of the ions in particular is an order of magnitude above the temperature increase in the island formation phase. This is by far the most intense process so far and only occurs upon island coalescence. If more coalescence events are produced, the conjecture is that more energy could be transferred to the particles as the current filaments merge successively.

Based on the scaling that the number of islands is proportional to the length to width ratio, a 256 x 16 system was set up, where the crossing angle of the field lines is now $\theta \simeq 7°$. To accomodate this geometry, the speed of light is given as $3\omega_{pe}$, while the electron and ion temperatures are slightly reduced at $v_{te} = 0.5\ \omega_{pe}\Delta$. The collisionless skin depth is then $c/\omega_{pe} = 3\Delta$, so that the y direction accomodates about as many skin-depths as in the 128 x 32 case. The particle size a and the Debye length are such that $a = \lambda_e = 0.5\Delta$. The β for this case is $\beta = 0.06$, while the gyrofrequencies are $\omega_{ce} = 1.17\ \omega_{pe}$ and $\omega_{ci} = 0.117\ \omega_{pe}$. The Alfven speed of $v_A \simeq 1\ \omega_{pe}\Delta$ yields

an Alfven transit time of 232 ω_{pe}^{-1} for the fundamental wavelength in

the x-direction. The quantity that best illustrates the island structure

of the system is the plasma current density. It is plotted in Fig. 13. Within

the compressional phase, this sheet tears into 16 islets. An illustration

of this at $\omega_{pe}t = 50$ is given in Fig. 13. The plasma is concentrated into

these islets. Successive coalescences keep taking place and only 3 islands

remain at $\omega_{pe}t = 100$. Finally at $\omega_{pe}t = 175$, the coalescence of the islands is

complete and one island pinned in the gap between the sheets prevails.

Vacuum appears elsewhere in the system. At $\omega_{pe}t = 325$, the coalesced

island comes up from the gap and begins traveling in the (negative) x-direction.

Note that the gap size is smaller than the final island size and also that since

many coalescences took place, the final momentum of the island may not necessarily

be zero in this case. A continuous energy increase is observed as the successive

coalescences take place. The levels reached when coalescence is complete are

an order of magnitude over those of the two-islands coalescence obtained with

a 128 x 32 system size, thereby confirming our conjecture.

The various cases presented in this section and in particular the

two-islands coalescence run are discussed next in terms of the energetics

of the interaction.

IV. Energy Transfer and Heating of Particles

This section is devoted to a study of the time evolution of the various components of the energy as a function of time. The analysis of various growing modes is also discussed. The evolution of the electron and ion temperatures is presented as well, including snapshots of the distribution functions.

For the stable case in the 32 x 32 system, Fig. 14(a) shows that the electrostatic energy dominates over the transverse electric energy. The electrostatic energy and the magnetic and kinetic energies of Fig. 14(b) all increase up to crow-bar approximately at t^2 since energy is imposed to the system as $\sin (t/4\tau_R)$ and stay nearly constant thereafter without any apparent exchange between them. Figures 14(c) and (d) show that the temperatures of both electrons and ions remain at the crow-bar level for the rest of the run. This behavior is also true in the high β 64 x 32 case, where the highest energies are achieved at crow-bar as shown in Figs. 15(a) and (b). The temperatures of Figs. 15(c) and (d) are, however, essentially thermal for the whole run. The topological modifications, i.e., attachment and detachment of the islands in the 64 x 32 β = 5 system, after crow-bar have little effect on the plasma heating.

The time history of the 64 x 32 run with β = 0.2 where snapping of the field lines occured, dragging the plasma into the o-point, is displayed in Fig. 16. The energies show a quick rise as the current is built up to its maximum in the plates. The energies are then approximately constant up to $\omega_{pe} t$ = 150, at which point they rise again, almost explosively, as we shall see later, to a new level. This is the snapping time when a vacuum develops at the center of the system. The energies oscillate about this level till the end of the run. The energy gain is supplied by the external circuit which maintains the sheet current; as the current concentrates in the islands the plasma inductance increases and a voltage drop develops which the driving currents do work against. The temperature plots of Fig. 16(c) and (d) show the preferential rise of electron and ion temperatures

in the y-direction at early times due to the strong early compression in that direction. When snapping occurs, it is the on-axis (x-component) temperature that increases preferentially for both electrons and ions. The directed energy acquired by the particles as the snapped field lines pull them into the o-point is dissipated into heat. Note the y-temperature reachieves the peak level that occured at crow-bar. The gain in on-axis temperature is a factor 3 for electrons and a factor 10 for ions over thermal at snapping.

A close examination of the energies per mode in the magnetic field displayed in Fig. 17 indicates that mode (0,1), i.e. ($k_x L_x/2\pi = 0$, $k_y L_y/2\pi = 1$), gains energy in the compressional phase and it is maintained at half the crow-bar level thereafter. The mode which grows at snapping is mode (1,0). The growth is faster than exponential and appears to be explosive with a scaling of $(t_o - t)^{-1}$ where $t_o = 160 \, \omega_{pe}^{-1}$. This behavior is associated with the rapid rise of the pinch effect as the driving currents do work against the voltage drop developed when the current concentrates in the islands. No other modes have significant magnetic field energies. These modes also achieve the highest energies at the same times in the electrostatic field. The level attained at snapping by the snapping mode (1,0) is equivalent to the crow bar level of the compressional mode (0,1) (Fig. 17).

We now discuss the case of a 128 x 32 system in which island coalescence occurs in terms of the energetics of the interaction. The energies and temperatures are displayed in Fig. 18. We also present distribution functions in Fig. 19. All energies increase sharply upon coalescence from $\omega_{pe}t = 200$ on. The kinetic energy gain at coalescence is a factor of 4 for electrons and a factor of 10 for ions over the value at the time of island formation. The magnetic energy increases dominate over the kinetic energy by a factor 5 because of the large vacuum region which must be filled with field. All energies oscillate after $\omega_{pe}t = 250$ with a pulsation period $\tau_p = 60 \, \omega_{pe}^{-1}$.

temperature in the x-direction (on-axis temperature) is a factor 9 over

thermal for the electrons and a factor of 60 for the ions. The y and z

directions get heating too but by a lesser amount. Note that when the center

island is formed the temperatures are still at the thermal level. Fig. 19

demonstrates that a hot tail is formed in the x-component of the momentum

in the coalesced state ($\omega_{pe}t = 325$), while the ions and electrons distributions

are essentially the original Maxwellian ones when the center island is formed

($\omega_{pe}t = 50$). Another noteworthy feature is the clear two-humped structure in

the ion distribution as coalescence occurs ($\omega_{pe}t = 225$) which illustrates

the two plasma streams (with opposite velocities) which correspond to the two

islands coming together.

The magnetic energy per mode as a function of time displayed in Fig. 20 shows

that only two modes gain significant energy. Mode (0,1), i.e. the fundamental

wavelength in the y-direction, grows as the center island is formed during the

compressional phase. It remains at about this level thereafter. Mode (1,0), however,

is the coalescence mode and corresponds to the fundamental wavelength in the

x-direction. It achieves a level an order of magnitude above the island

formation mode one and oscillates after $\omega_{pe}t = 250$ with a period of 60 ω_{pe}^{-1}

as do all the energies. The growth of mode (1,0) is faster than exponential

and the magnetic energy scales like $(t_o - t)^{-1}$ with $t_o \simeq 250 \ \omega_{pe}^{-1}$, i.e.,

it is again quasi-explosive as in the snapping case.

We can estimate the kinetic energy gain of the particles from the work done

by the J x B forces on the current filaments as they approach each other. The

force between the two currents is

$$F = 2I^2/c^2 \ \frac{1}{y} , \tag{5}$$

where y is the distance between the two filaments.

The work done to bring the filaments from the initial separation y_s to the coalescence separation y_c yields the loss in potential energy ΔU:

$$\Delta U = \int_{y_c}^{y_s} 2I^2/c^2 \; \frac{1}{y} \, dy = 2I^2/c^2 \ln \; (y_s/y_c) \sim 2I^2/c^2, \qquad (6)$$

since the current is forced to remain approximately constant as the current filaments approach in the simulation. This is the energy available to the particles. For the simulation parameters, this yields $\Delta U = 330 \; N_o \; \kappa T_{eo}$, where N_o is the total number of particles. The measured total kinetic energy gain ΔW in the coalescence phase is $\Delta W = 1/6 \; \Delta U \simeq 60 \; (N_o \; \kappa T_{eo})$. The remainder of the available potential energy $(5/6 \; \Delta U)$ released by the two coalescing fila-ments goes into field energy and in fact the overall energy increase closely balances the calculated potential energy loss. The electrons and ions get about equal amounts. The ion kinetic energy increase ΔW_i over the island formation phase is $\Delta W_i = 30 \; (N_o \; \kappa T_{eo})$. The average coalescence velocity v_c measured in the simulation is $v_c = 1.7 \; v_{te}$, in agreement with the above ion kinetic energy increase so that $\Delta W_i \simeq M \; v_c^2$. If all of this directed energy is converted into heat, the temperature gain will be

$$\kappa \Delta T = \Delta W_i/N_o \simeq 30 \; \kappa T_{eo}, \qquad (7)$$

which is in reasonable agreement with the on-axis ion temperature increase over the island formation phase of Fig. 18 measured in the simulation. Since ions and electrons tend to move in unison as the islands coalesce, if the mass ratio had been much larger than the one used here, the ion energy gain might have been much more than the electron gain.

The oscillations in the energies (see Fig. 18) after coalescence are attributed to the breathing of the coalesced island: the island becomes more

oblate to more round from time to time due to the overshoot of the two colliding plasmas. These breathing oscillations are essentially the fundamental compressional Alfven mode. The frequency of the pulsation may be simply estimated as $k \, v_A$, where $k = 2\pi/\lambda \sim 2\pi/d$, d being the island diameter. In our simulation, the island magnetic field is of the order of the original near-sheet value so that $\omega_{ce} = 0.75 \, \omega_{pe}$ and the maximum island plasma density is about 5 times its initial value, while the island diameter $d \sim 32 \, \lambda_e$. The estimated pulsation period then is $\tau_p \sim 60 \, \omega_{pe}^{-1}$, in agreement with the observed period of the pulsation.

The energies and temperatures for the multiple coalescence 256 x 16 case are displayed in Fig. 21. All energies and temperatures increase steadily as the successive coalescences take place. The levels reached at $\omega_{pe} t = 200$ where coalescence is complete are an order of magnitude over those of the two-islands coalescence obtained with a 128 x 32 system size. Repeated coalescence culminates in an ion-temperature increase in the x-direction by two orders of magnitude over thermal. In comparison, the energies and temperatures achieved when the neutral sheet tears into 16 islets are only twice the initial ones. The sudden decrease of the energies at $\omega_{pe} t = 300$ corresponds to the escape of the coalesced island from the gap between the sheets.

V. Conclusions and Discussion

We have investigated magnetic x-point dynamics through fully self-consistent particle simulations. The results we have obtained by the particle method show intricate differences from the conventional MHD pictures and, at the same time, present surprisingly similar overall physical pictures to what MHD simulations or theories suggest. We should first emphasize that our simulation spatial scale is relatively small, i.e. only several times the electron collisionless skin depth and ions are not strongly magnetized; on the other hand, the conventional MHD simulation or theory deals with zero collisionless skin depth and Larmor radius situations and, therefore, intends to be applicable to a larger scale structure. The relatively small ratio of the simulation spatial scale to the Debye length as compared with an ordinary laboratory plasma may make the electrostatic interaction much more important.

In our simulations the magnetic field penetration toward the separatrix from the external current sheet areas is associated with a charge separation. The physical picture we obtained is: the electrons are quickly kicked inward by the magnetic field pressure; their motion is that associated with the E x B drift produced by the inductive electric field E_z. This motion sets up a charge separation and the resultant electrostatic field drags the ions inward. The ions do not follow the E x B motion because they cannot complete a gyro-orbit in the sheath layer of the penetrating fields. The electrostatic field gives rise to an E_y x B_x drift for the electrons; this drift produces a return current in the z-direction which constitutes a diamagnetic shielding. As already mentioned, the ions do not partake of the E x B motion because of their large Larmor radii and thus do not cancel the electron current. The picture is similar to that of the Rosenbluth sheath.[35]

The magnetic flux easily goes through the x-point without changing the topology for a crossing angle of 90° in our particle simulations. On the other hand, the flux does not cross the x-point for a 90° angle when a similar simulation is carried out[36] on an almost (i.e. except for small numerical dissipations) dissipationless MHD particle code.[37] This suggests that the magnetic field reconnection at a 90° x-point probably depends strongly on the ratio of x-point (or o-point) scale length to the collisionless skin depth (and/or the ion Larmor radius): if this ratio is not very large, the magnetic flux does not have much difficulty in penetrating through an x-point as is the case in our particle simulations.

When the crossing angle is substantially less than 90°, the magnetic field topology is unstable as the flux is driven in from the current sheet area toward the x-point. The field lines snap at the x-point and two y-points are formed; then a vacuum region develops at the original x-point location. When the geometry is very thin, i.e, the crossing angle is very small, many magnetic x- and o-points (islands) are induced in the neutral sheet area (collisionless tearing instability). It is interesting to note that the initial magnetic field lines are predominantly parallel to the external sheets, i.e. in the x-direction, except near the gap, while the final magnetic field lines are primarily perpendicular to the sheets, i.e. in the y-direction (see Fig. 11). This tendency is even more prominent for the case corresponding to Fig. 13 (field lines are not shown in this case). We have found for the cases where such islands are formed that (i) a large amount of magnetic energy conversion into kinetic energy takes place when magnetic islands coalesce, while much less energy conversion happens through the tearing instability or island formation phase; (ii) the explosive energy conversion associated with island coalescence goes to the creation of

extremely hot ions; (iii) after islands merging the coalesced island pulsates
and eventually the oscillations dissipate into heat. We note that although the
above findings came from particle simulations, they show many features in common
with MHD studies[38] in terms of the resulting physical picture of the island
coalescence phase. This is somewhat surprising, since the MHD study has zero
Larmor radius and zero collisionless skin depth, while in the particle simula-
tion the ion Larmor radius for the hot ions created by the merging is very large,
practically infinite; the ions are, however, confined electrostatically.

The large kinetic energy release as a result of coalescence may be looked
upon as a case of the bifurcation phenomenon: the two states correspond to
the original higher potential energy state and to the final lower potential energy
state. The path between the initial and final states involves magnetic flux
penetration, the appearance of the neutral sheet, snapping of field lines, for-
mation of vacuum regions and magnetic islands, coalescence of the islands,
breathing of the island and dissipation of the oscillatory energy of the coalesced
islands.

The experiments of Stenzel and Gekelman[18] have shown a number of similarities
and some differences with these simulations. A close correspondence of results
should not be expected due to differences in parameters but some comments are
worth making. Their experiments have only very weak magnetic fields along the
external current direction (weaker than the current-generated fields). They have
observed similar field-line snapping and formation of two y-points but have not
observed a very low density or vacuum region. This is probably due to the fact
that their lowest plasma β is of the order 1; for high β's we also do not
see a vacuum region. We have runs with β much less than 1, which case tends
to yield stronger trapping of the plasma in the o-points. They also have
continuous plasma generation by ionization which will tend to fill in the low

plasma density regions. Their geometry of the x-point is 75(cm) x 32(cm), almost a 2 to 1 ratio. This is the only ratio for which they have made experiments. Sometimes they see induced small islands in the middle, which seems to correspond to our Fig. 6. Flow patterns as well as distribution functions are relatively similar to our cases of no island merging. They have not observed strong tail heating, only some bulk heating. Again, this is consistent with our results that unless o-points merging takes place, there is neither intense heating nor hot tail information. The experiments are primarily in the collisional regime (S ~ 20), while the simulation magnetic Reynolds number S ≃ 800. The experimental collisionless skin depth is 0.6 cm some 1/50 of the driving sheet currents separation, while the ratio for the simulations is 1/6. The experiments are, of course, three dimensional while the simulations are two dimensional with no variation being allowed in the driving current direction. Overall then, the physical phenomena observed in their experiments and in our simulations are consistent and compatible.

There is, in addition, one experiment on merging of two current carrying plasma columns[39] which shows production of energetic ions upon merging at the expense of magnetic energy. This experiment would correspond to our two-islands coalescence simulation except that the preferential direction of particle acceleration is antiparallel to the plasma currents in the experiment whereas it is perpendicular to the currents in our simulation.

As we have seen extremely energetic tails in the ions and electrons distributions are generated as a result of the magnetic island merging. This process may be involved in such phenomena as the solar flares and the geomagnetic sub-storms associated with island formation and merging in the deep tail. It is also conceivable that not only growth of one island but coalescence of many (equivalent

to coupling of many tearing modes) could play a role in major disruptions observed in tokamaks; this process may also play a role in the initial formation of the current channel in these devices with break-up of the skin current into islands and their recoalescence in the center of the discharge. The physics of island coalescence in a tokamak may, however, be different from the coalescence process studied in the present paper, because the plasma near the neutral sheet in our case is compressible due to the lack of toroidal field; incompressibility is a safe approximation for most of the theoretical work[4,6] dealing with the presence of a strong toroidal field. Another difference is that the Larmor radius near the neutral sheet is large, of the order of the sheet thickness in our case, while the Larmor radius is small in tokamaks because of the toroidal field.

The strong ion heating which occurs during coalescence and the high temperature that results in the merged state suggests a scheme for hot plasma production in a multipole or Doublet-type configuration. By manipulation of the shaping coils, two or more plasma current filaments could be established and then induced to merge, thereby producing a very hot plasma. Assuming the experiment can be done, our estimates for typical Doublet-III parameters - toroidal field 26kG, plasma density 10^{13}-10^{14} (cm^{-3}), the ohmic temperature 0.5-1kev, and plasma current 1-2MA - indicate that a doubling of the temperature is feasible on impact. Similar ideas have been put forth by Shafranov[40] and Ohyabu et al.[41]. From our simulations, we predict that the kinetic energy of the islands increases as the islands are accelerated under the magnetic attraction; upon merging (or inelastic collision with the other island) the ordered kinetic energy gained becomes randomized through mixing of the plasma from both islands. The dissipation of the ordered motion is not instantaneous as it can take place only as the field lines of the two islands reconnect allowing plasma to flow from one to

the other. The actual coalescence is accompanied by damped oscillations. The technology of heating a plasma by this means might be simplified by doing it in small steps, i.e. forming many small current carrying plasma tori and merging them with a larger one in succession.

References

1. E. N. Parker, Cosmical Magnetic Fields, Clarendon Press, Oxford, (1979).

2. V. M. Vasyliunas, Rev. Geophys. Space Phys. 13, 303 (1975).

3. G. Bateman, MHD Instabilities, The MIT Press, Cambridge, Mass., (1978).

4. H. P. Furth, J. Killeen and M. N. Rosenbluth, Phys. Fluids, 6, 459 (1963).

5. J. W. Dungey, Cosmic Electrodynamics, Cambridge University Press, Cambridge, (1958).

6. P. H. Rutherford, Phys. Fluids, 16, 1903 (1973).

7. G. Laval, R. Pellat, and M. Vuillemin in Plasma Physics and Controlled Nuclear Fusion Research (International Atomic Energy Agency, Vienna, 1965), Vol. III, p. 259.

8. B. Coppi, G. Laval and R. Pellat, Phys. Rev. Lett. 16, 1207 (1966).

9. J. F. Drake and Y. C. Lee, Phys. Rev. Lett. 39, 453 (1977).

10. J. F. Drake and Y. C. Lee, Phys. Fluids, 20, 1341 (1977).

11. S. Von Goeler, W. Stodiech, N. Sauthoff, Phys. Rev. Lett. 33, 1201 (1974).

12. S. V. Mirnov and I. B. Semenov, Zh. Eksp. Teor. Fiz. 60, 2105 (1971) [Sov. Phys. JETP 33, 1134 (1971)].

13. R. L. McPherron, Rev. Geophys. Space Phys. 17, 657 (1979).

14. P. T. Baum and A. Bratenahl, J. Plasma Phys. 18, 257 (1977).

15. S. I. Syrovatskii in Proceedings of the P. N. Lebedev Physical Institute (Consultants Bureau, New York, 1976), 74, 1.

16. J. H. Irby, J. F. Drake, and H. R. Griem, Phys. Rev. Lett., 42, 228 (1979).

17. R. L. Stenzel and W. Gekelman, Phys. Rev. Lett. 42, 1055 (1979).

18. R. L. Stenzel, and W. Gekelman, University of California at Los Angeles Plasma Physics Group Report No. 453 (1979). W. Gekelman and R. L. Stenzel, University of California at Los Angeles Plasma Physics Group Reports No. 463, 466 and 467 (1980), unpublished.

19. M. A. Cross and G. Van Hoven, Phys. Rev. A $\underline{7}$, 1347 (1973).

20. M. N. Rosenbluth, D. A. Monticello, H. Strauss, and R. B. White, Phys. Fluids, $\underline{19}$, 1987(1976); B. V. Waddell, D. A. Monticello, M. N. Rosenbluth and R. B. WHite, Nucl. Fusion $\underline{16}$, 528 (1976).

21. R. B. White, D. A. Monticello and M. N. Rosenbluth, Phys. Rev. Lett. $\underline{39}$, 1618 (1977).

22. J. M. Finn, Phys. Fluids $\underline{20}$, 1749 (1977).

23. B. Carreras, H. R. Hicks, J. A. Holmes, and B. V. Waddell, Phys. Fluids $\underline{23}$, 1811 (1980).

24. A. Sykes and J. A. Wesson, Phys. Rev. Lett. $\underline{44}$, 1215 (1980).

25. J. M. Finn and P. K. Kaw, Phys. Fluids $\underline{20}$, 72 (1977).

26. P. L. Pritchett and C. C. Wu, Phys. Fluids $\underline{22}$, 2140 (1979).

27. D. Biskamp and H. Welter, Phys. Rev. Lett. $\underline{44}$, 1069 (1980).

28. T. Sato, T. Hayashi, T. Tamao and A. Hasegawa, Phys. Rev. Lett. $\underline{61}$, 1548 (1978); T. Hayashi and T. Sato, J. Geophys. Res. $\underline{83}$, 217 (1978). T. Sato and T. Hayashi, Phys. Fluids $\underline{22}$, 1189 (1979).

29. D. O. Dickman, R. L. Morse and C. W. Nielson, Phys. Fluids, $\underline{12}$, 1708 (1969).

30. A. T. Lin, Phys. Fluids $\underline{21}$, 1026 (1978).

31. I. Katanuma and T. Kamimura, Phys. Fluids $\underline{23}$, 2500 (1980).

32. J. Busnardo-Neto, P. L. Pritchett, A. T. Lin and J. M. Dawson, J. Compt. Phys. $\underline{23}$, 300 (1977); C. W. Nielson and H. Ralph Lewis, Methods in Computational Physics (Academic Press, New York, 1976), Vol. 16, p. 367.

33. A. T. Lin, J. M. Dawson and H. Okuda, Phys. Fluids $\underline{17}$, 1995 (1974); A. B. Langdon and B. F. Lasinski, Methods in Computational Physics (Academic Press, New York, 1976), Vol. 16, p. 327.

34. C. K. Birdsall, A. B. Langdon and H. Okuda, Methods in Computational Physics (Academic Press, New York, 1970), Vol. 9, p. 241.

35. M. N. Rosenbluth in Magnetohydrodynamics: A Symposium (Stanford University, Stanford, California, 1957), Vol. 1, p. 62; M. G. Haines, Nucl. Fusion 17, 811 (1977).

36. F. Brunel, T. Tajima and J. M. Dawson, Bulletin of the American Physical Society, 25, 884 (1980).

37. F. Brunel, J. N. Leboeuf, T. Tajima, J. M. Dawson, M. Makino and T. Kamimura, submitted to Journ. Compt. Phys. [University of California at Los Angeles Plasma Physics Group Report No. 512 (1980)].

38. C. C. Wu, J. N. Leboeuf, T. Tajima and J. M. Dawson, submitted to Phys. Rev. Lett. [University of California at Los Angeles Plasma Physics Group Report No. 511 (1980)].

39. S. Besshou and M. Kawashima, in Proceedings of the Fourth International Conference on Plasma Physics, Nagoya (Nagoya University, Nagoya, Japan, 1980), Vol. II, Paper 9a - I - 05.

40. V. D. Shafranov, Nucl. Fusion 19, 187 (1979).

41. N. Ohyabu, C. L. Hsieh and T. H. Jensen, J. Plasma Phys. 21, 253 (1979).

Acknowledgements

Figure Captions

Fig. 1 a) External x-point geometry magnetic field lines for a 64 x 32

system. b) Linear variation of the x-component of the external

magnetic field as a function of the distance between sheets in the

y-direction. c) Space integrated external (J_{ext}) and return

plasma (J_p) currents in the z-direction as a function of time. The

sheet current is crow-barred at $\omega_{pe}t = 31.4$.

Fig. 2 32 x 32 stable configuration magnetic field lines. The vacuum

x-point field is displayed in the top left inset. The total field

lines are displayed at $\omega_{pe}t = 5$, 30 and 85. The plasma β is 0.07.

Fig. 3 Left hand side: 32 x 32 stable configuration ion density at $\omega_{pe}t = 5$,

35 and 80. The dotted contours indicate levels below the average

density at a particular time, the full contours level above. Com-

pression up to 3 times the initial density is achieved as the current

rises in the plates. Right hand side: 32 x 32 stable configuration

plasma current density at $\omega_{pe}t = 5$, 15, 25 and 80. The dotted contours

indicate regions of highest plasma return current in the negative

z-direction.

Fig. 4 32 x 32 stable configuration electric field and mass flow. The

electrostatic field is displayed on the left at $\omega_{pe}t = 15$ and 35;

the mass flow on the right at $\omega_{pe}t = 15$ and 30.

Fig. 5 Test particle orbits in the 32 x 32 stable case. The dots represent

the (x, y) coordinate of the particles at each instant of time from

crow-bar ($t = 31.4\ \omega_{pe}^{-1}$) to 200 ω_{pe}^{-1} in steps of 5 ω_{pe}^{-1}. The

position of the particles at crow-bar is indicated by an x for an

electron or an ion originally at the x-point and by an o for an electron

or an ion originally at the o-point in the gap between the sheets.

Fig. 6   64 x 32 unstable configuration magnetic field lines for β = 5.0.

The top left inset represents the vacuum x-point field.   The

total field is displayed at $\omega_{pe}t$ = 20, 40, 60, 80 and 100.

Fig. 7   Magnetic field lines for the 64 x 32 system and β = 0.2 or

snapping case.   From top to bottom: vacuum x-point field and

total field at $\omega_{pe}t$ = 30 (neutral sheet formation phase), 90

150 (snapped field lines configuration) and 300.

Fig. 8   Left hand side: Ion density in the snapping case at $\omega_{pe}t$ = 30, 90, 150

and 300.   The dotted curves represent levels below the average density

at each time, the full curves level above.   A vacuum is established

throughout the system except at the o-point where the density is com-

pressed up to 5 times the initial density.   Right hand side:

Plasma current density in the z-direction at equivalent times.   The

dotted contours represent regions of highest (negative) return current.

Fig. 9   Electrostatic field and mass flow vector field plots in the snapping

case with β = 0.2 at $\omega_{pe}t$ = 30, 90, 150 and 300.   The electrostatic

field acts to drag the ions into the x-point up to crow-bar, into the

o-point later on and to confine them at the o-point in the gap between

the sheets thereafter.   The bold arrows emphasize the electrostatic

field and mass flow directions.

Fig. 10   Test particle orbits in the snapping case.   The dots represent the

(x, y) coordinate of the particles at each instant of time from

0 to 300 ω_{pe}^{-1} in steps of 5 ω_{pe}^{-1}.   The initial position of the

particles is indicated by an x for an electron or an ion originally

at the x-point and by an 0 for an electron or an ion originally at

the o-point in the gap between the sheets.

Fig. 11   128 x 32 island coalescence run: Magnetic field lines. From top

to bottom, vacuum x-point field and total field at $\omega_{pe}t$ = 50 (island

formation phase), 125 (saturated island phase), 250 (coalescence phase)

and 375 (merged phase). The plasma β = 0.2.

Fig. 12   128 x 32 island coalescence run. The ion density is displayed on the

left at, from top to bottom, $\omega_{pe}t$ = 50, 125, 250 and 375. The dotted

contours represent levels below the average density at a particular

time, full contours levels above. The plasma current density in the

z-direction is shown on the right at equivalent times. Dotted contours

indicate regions of highest return current.

Fig. 13   256 x 16 coalescence run. The plasma current density in the z-direction

or return current is displayed at $\omega_{pe}t$ = 25 (neutral sheet), 50

(16 islets are formed), 100 (repeated coalescence yields 3 islands),

125 (two islands stage through further coalescence) and 225 (one island

in the gaps between the sheets). The plasma β = 0.06 and Δ = 2 λ_e.

The dotted curves represent regions of maximum return plasma (negative)

current.

Fig. 14   32 x 32 stable configuration. Time evolution of a) the magnetic

energy (full curve), electrons kinetic energy (crosses) and ions kinetic

energy (circles); b) the electrostatic (full curve) and transverse

electric (crosses) energies; c) the electrons temperature in the

x (full curve), y (crosses) and z (circles) directions; d) the ion

temperature in the x (full curve), y (crosses) and z (circles) directions.

Fig. 15   64 x 32 β = 5 case. Time evolution of a) the magnetic energy (full

curve), electrons kinetic energy (crosses) and ions kinetic energy

(circles); b) the electrostatic (full curve) and transverse electric

(crosses) energies; c) the electrons temperature in the x (full curve),

y (crosses) and z (circles) directions; d) the ions temperature in the

x (full curve), y (crosses) and z (circles) directions.

Fig. 16 64 x 32 β = 0.2 snapping case. Time evolution of a) the magnetic energy (full curve), electrons kinetic energy (crosses) and ions kinetic energy (circles); b) the electrostatic (full curve) and transverse electric (crosses) energies; c) the electrons temperature in the x (full curve), y (crosses) and z (circles) directions; d) the ions temperature in the x (full curve), y (crosses) and z (circles) directions.

Fig. 17 64 x 32 β = 0.2 snapping case. Magnetic mode energies as a function of time a) growing mode $k_x L_x / 2\pi$ = 0, $k_y L_y / 2\pi$ = 1 or mode (0, 1) in the compressional phase; b) snapping mode $k_x L_x / 2\pi$ = 1, $k_y L_y / 2\pi$ = 0 or mode (1, 0).

Fig. 18 128 x 32 coalescence run with β = 0.2. Time evolution of a) the magnetic energy (full curve), electrons kinetic energy (crosses) and ions kinetic energy (circles); b) the electrostatic (full curve) and transverse electric (circle) energies; c) the electrons temperature in the x (full curve), y (crosses) and z (circles) directions; d) the ions temperature in the x (full curves), y (crosses) and z (circles) directions.

Fig. 19 128 x 32 coalescence run with β = 0.2. a) electrons and b) ions distribution functions in the x-direction at $\omega_{pe} t$ = 50 (full bold curve; island formation phase), $\omega_{pe} t$ = 225 (dotted curve; coalescence phase) and $\omega_{pe} t$ = 325 (full thin curve, merged state).

Fig. 20 128 x 32 coalescence run with β = 0.2. Magnetic mode energies as a function of time a) growing mode $k_x L_x / 2\pi$ = 0, $k_y L_y / 2\pi$ = 1 in the island formation phase; b) coalescence mode $k_x L_x / 2\pi$ = 1, $k_y L_y / 2\pi$ = 0. The pulsation period of the coalescence mode is τ_p = 60 ω_{pe}^{-1}.

Fig. 21   256 x 16 coalescence run with β = 0.06. Time evolution of a) the

magnetic energy (full curve), the electrons kinetic energy (crosses)

and the ions kinetic energy (circles); b) the electrons temperature

in the x (full curve), y (crosses) and z (circles) directions;

c) the ions temperature in the x (full curve), y (crosses) and z

(circles) directions.

X-POINT FIELD
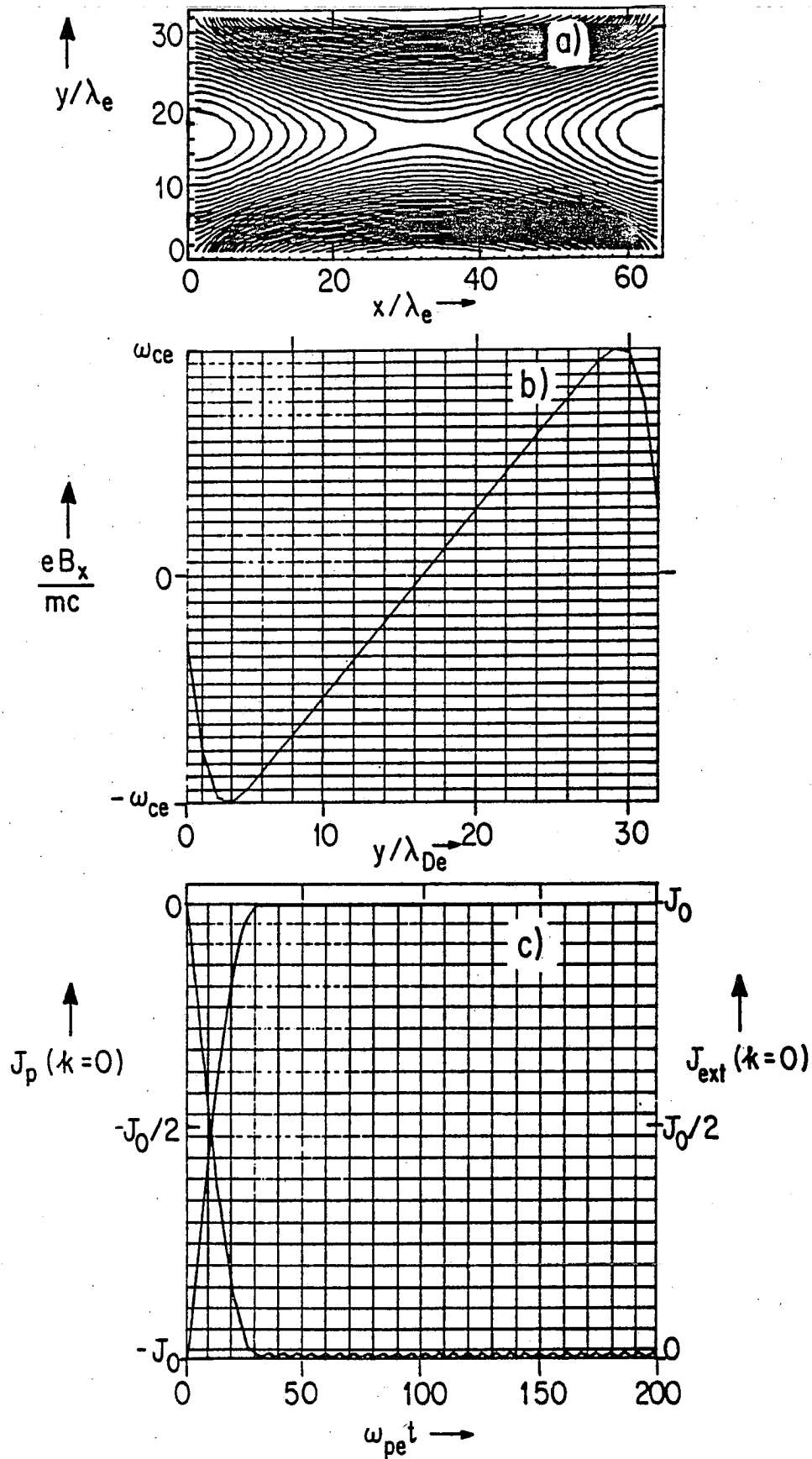
Figure 1

# MAGNETIC FIELD LINES
$\beta = 0.07$

EXTERNAL FIELD $\omega_{pe}t = 30$
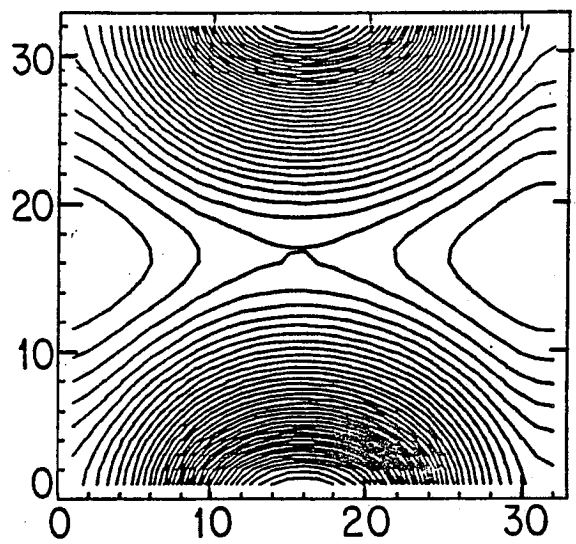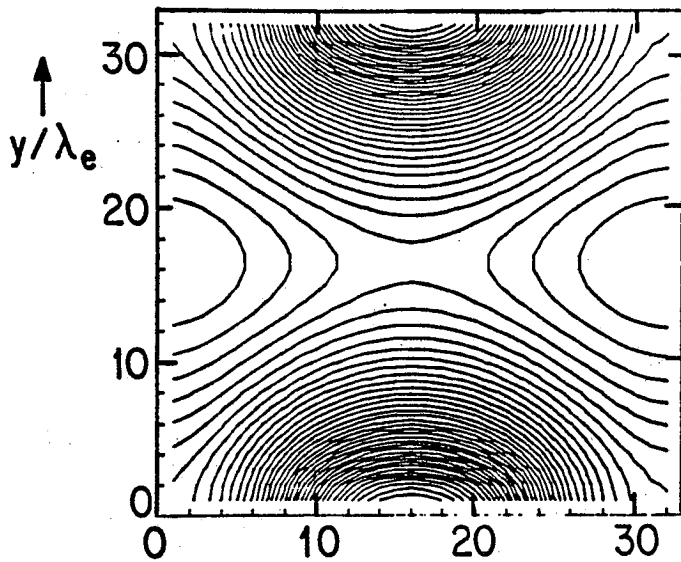
TOTAL FIELD $\omega_{pe}t = 5$ $\omega_{pe}t = 85$

Figure 2

ION DENSITY
$\beta = 0.07$

PLASMA CURRENT DENSITY
$\beta = 0.07$

$\omega_{pe} t = 5$

$\omega_{pe} t = 5$

$\omega_{pe} t = 15$

$\omega_{pe} t = 15$

$\omega_{pe} t = 35$

$\omega_{pe} t = 25$

$\omega_{pe} t = 80$

$\omega_{pe} t = 80$

y/λ_e

x/λ_e
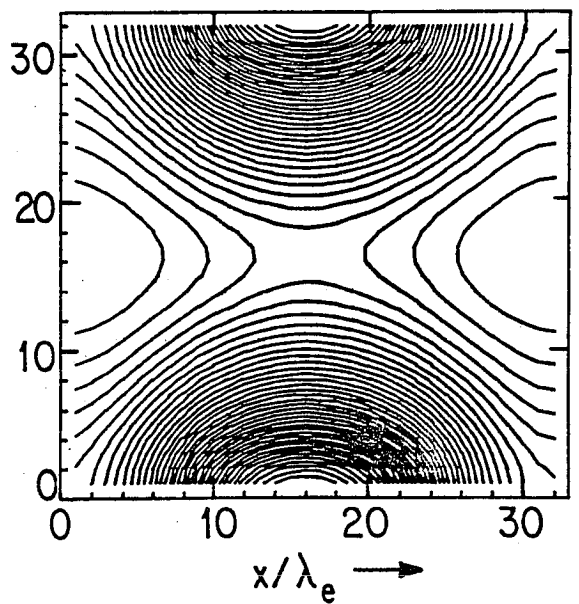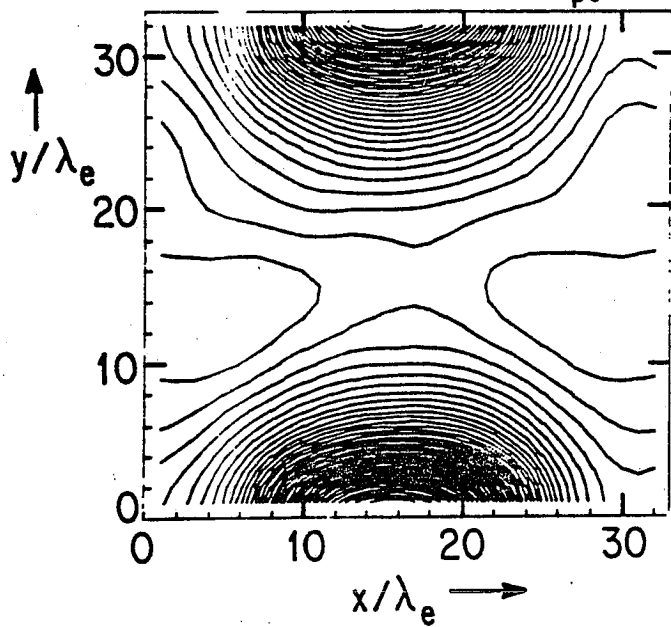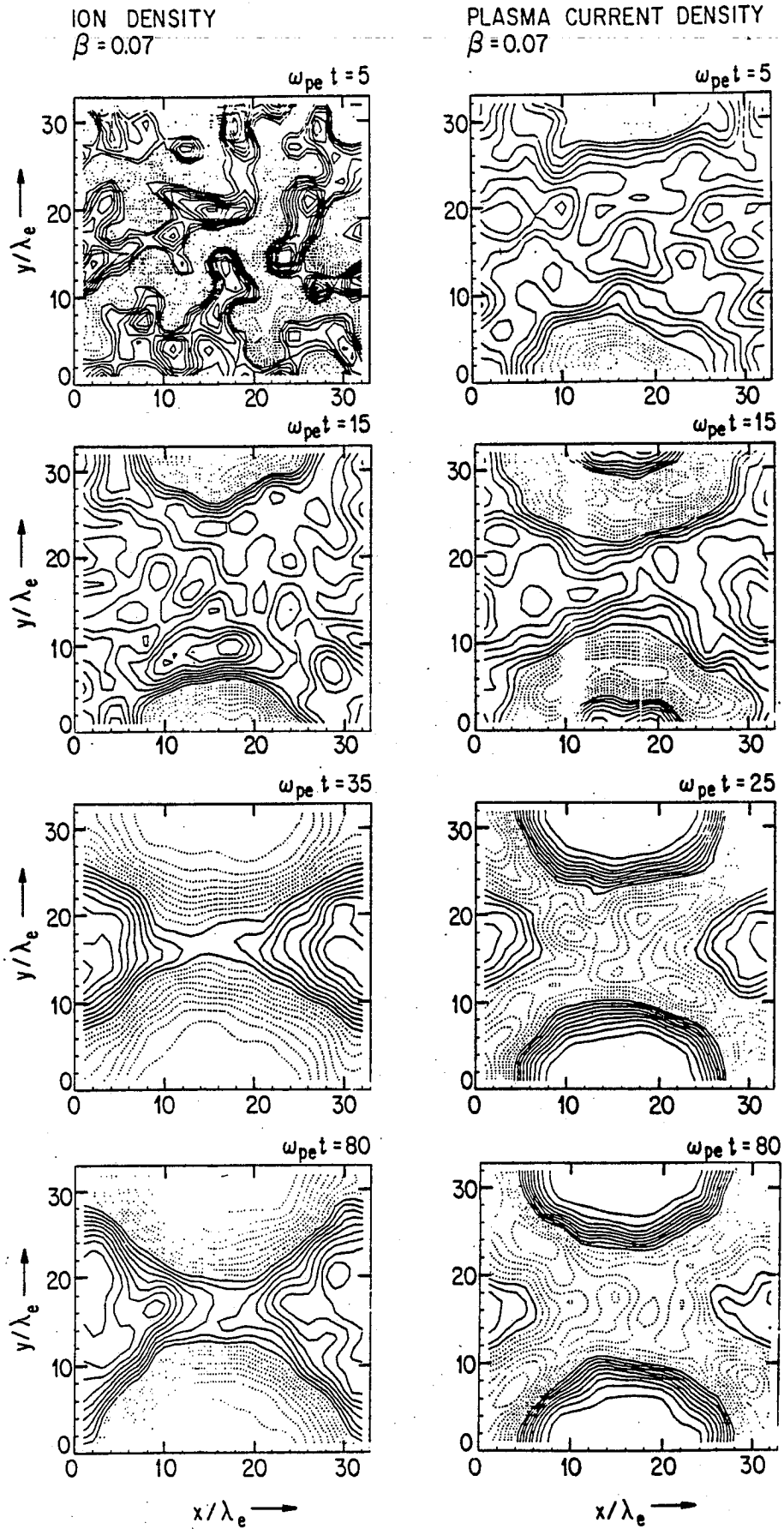
Figure 3

ELECTROSTATIC FIELD AND MASS FLOW

$\beta = 0.07$
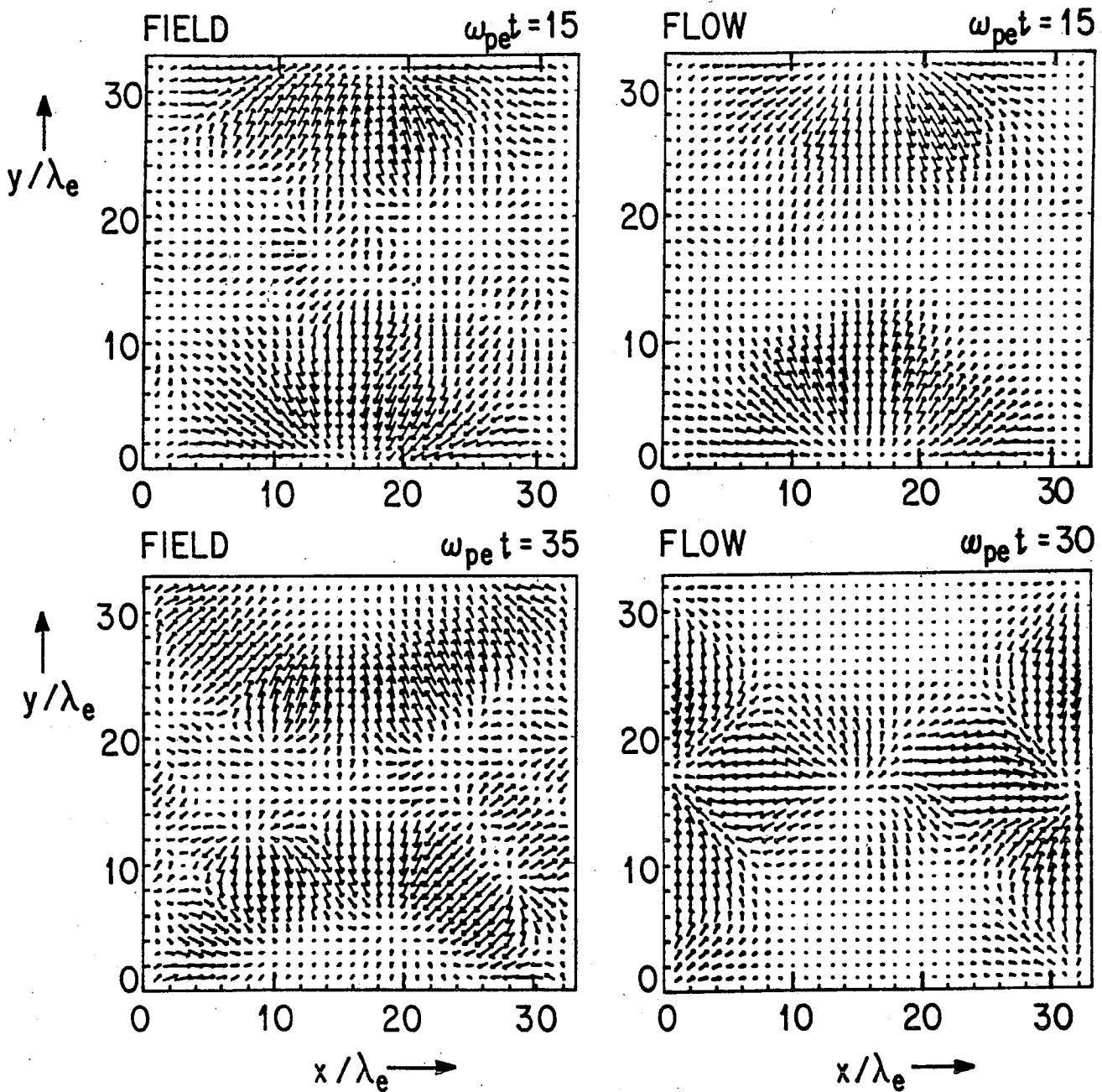
Figure 4

TEST PARTICLE ORBITS
$\beta = 0.07$
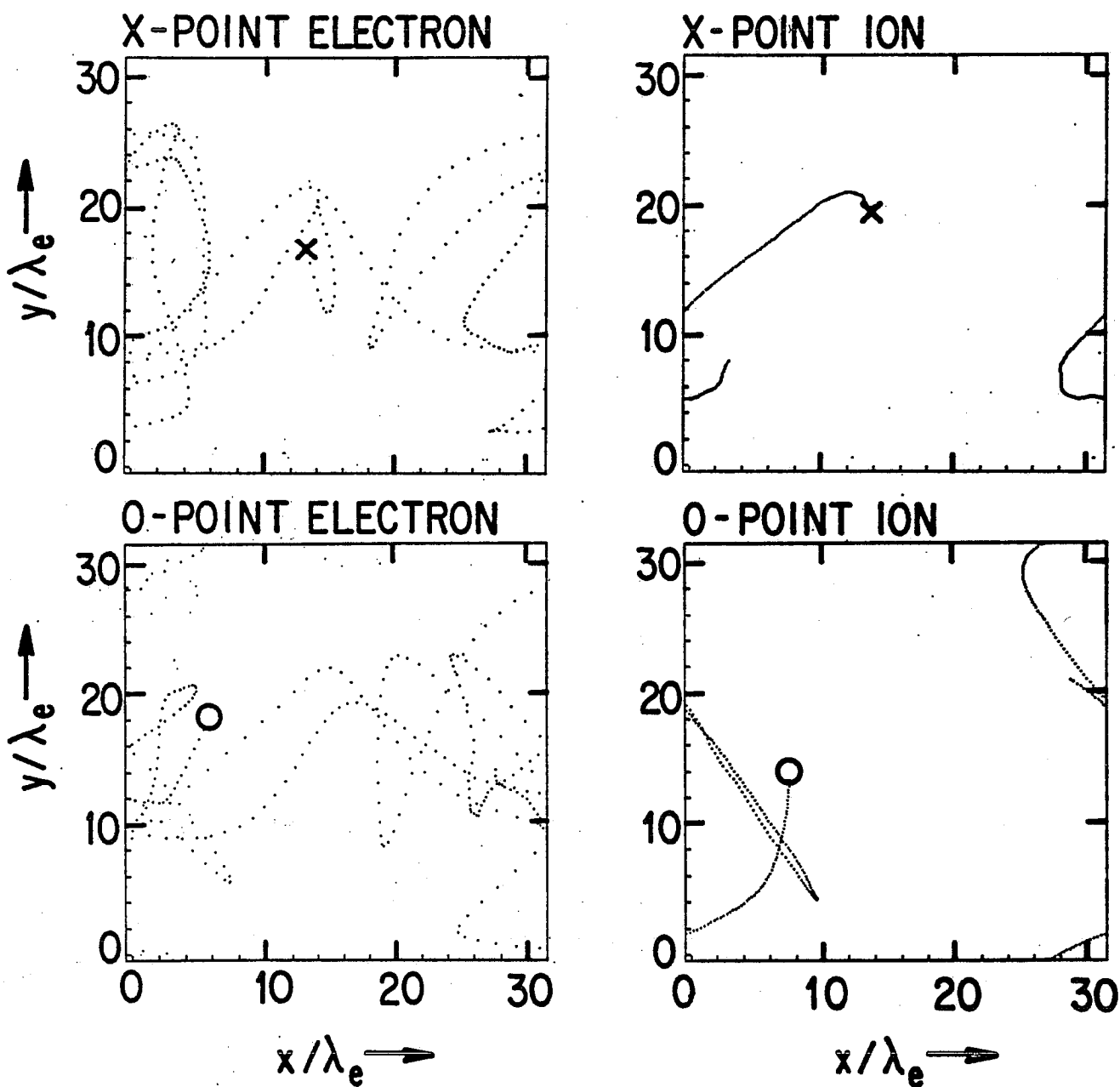
Figure 5

MAGNETIC FIELD LINES
BETA = 5.0
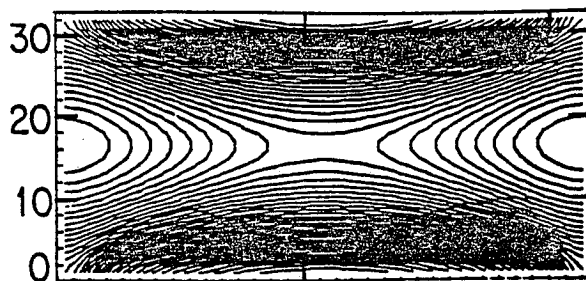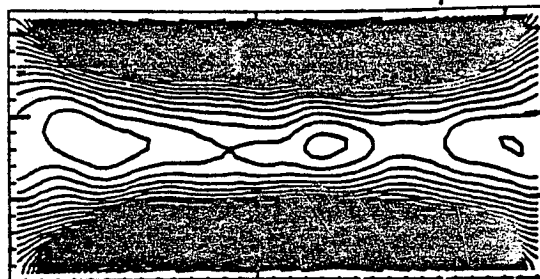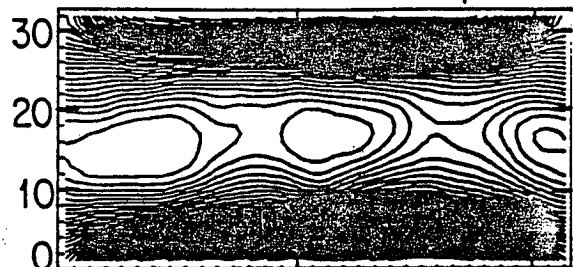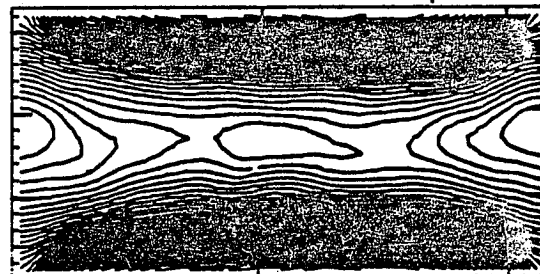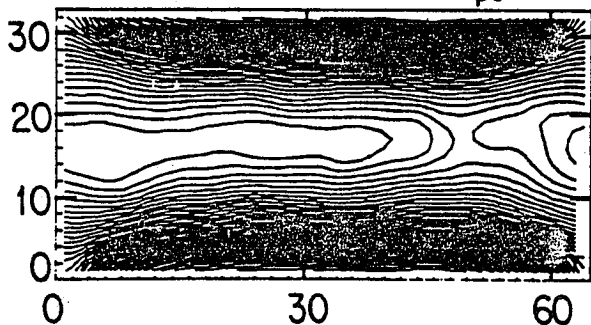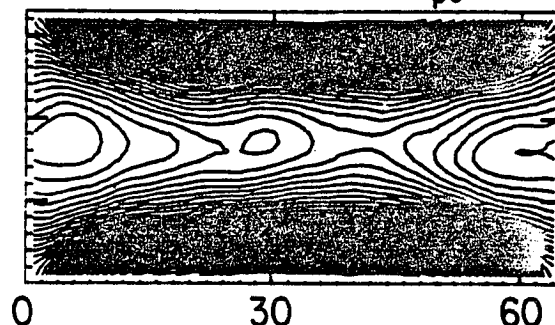
Figure 6

MAGNETIC FIELD LINES
$\beta = 0.2$

EXTERNAL FIELD

TOTAL FIELD $\omega_{pe}t = 30$

$\omega_{pe}t = 90$

$\omega_{pe}t = 150$

$\omega_{pe}t = 300$
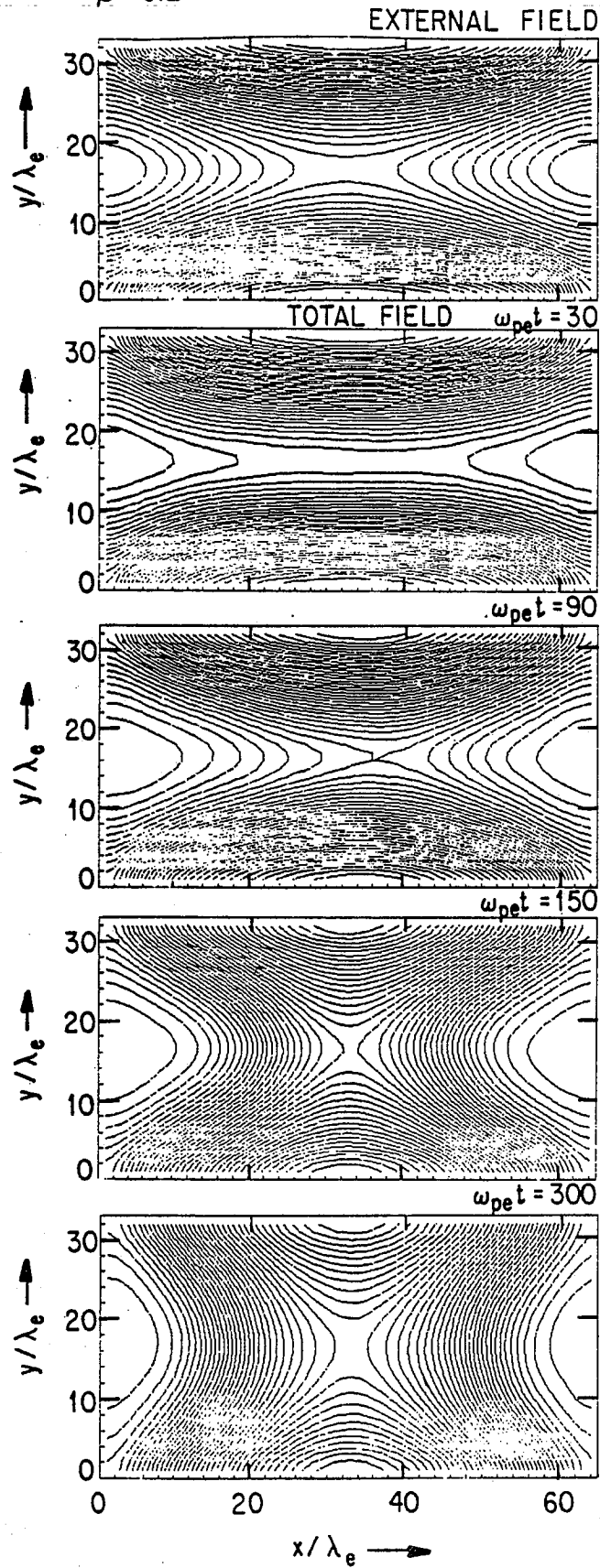
Figure 7

ION DENSITY
$\beta = 0.2$

PLASMA CURRENT DENSITY
$\beta = 0.2$

$\omega_{pe}t = 30$

$\omega_{pe}t = 30$

$\omega_{pe}t = 90$

$\omega_{pe}t = 90$

$\omega_{pe}t = 150$

$\omega_{pe}t = 150$

$\omega_{pe}t = 300$

$\omega_{pe}t = 300$

$x/\lambda_e \longrightarrow$

$x/\lambda_e \longrightarrow$

Figure 8

ELECTROSTATIC FIELD
$\beta = 0.2$

$\omega_{pe}t = 30$

$\omega_{pe}t = 90$

$\omega_{pe}t = 150$

$\omega_{pe}t = 300$

$x/\lambda_e \longrightarrow$

MASS FLOW
$\beta = 0.2$

$\omega_{pe}t = 30$

$\omega_{pe}t = 90$

$\omega_{pe}t = 150$

$\omega_{pe}t = 300$

$x/\lambda_e \longrightarrow$
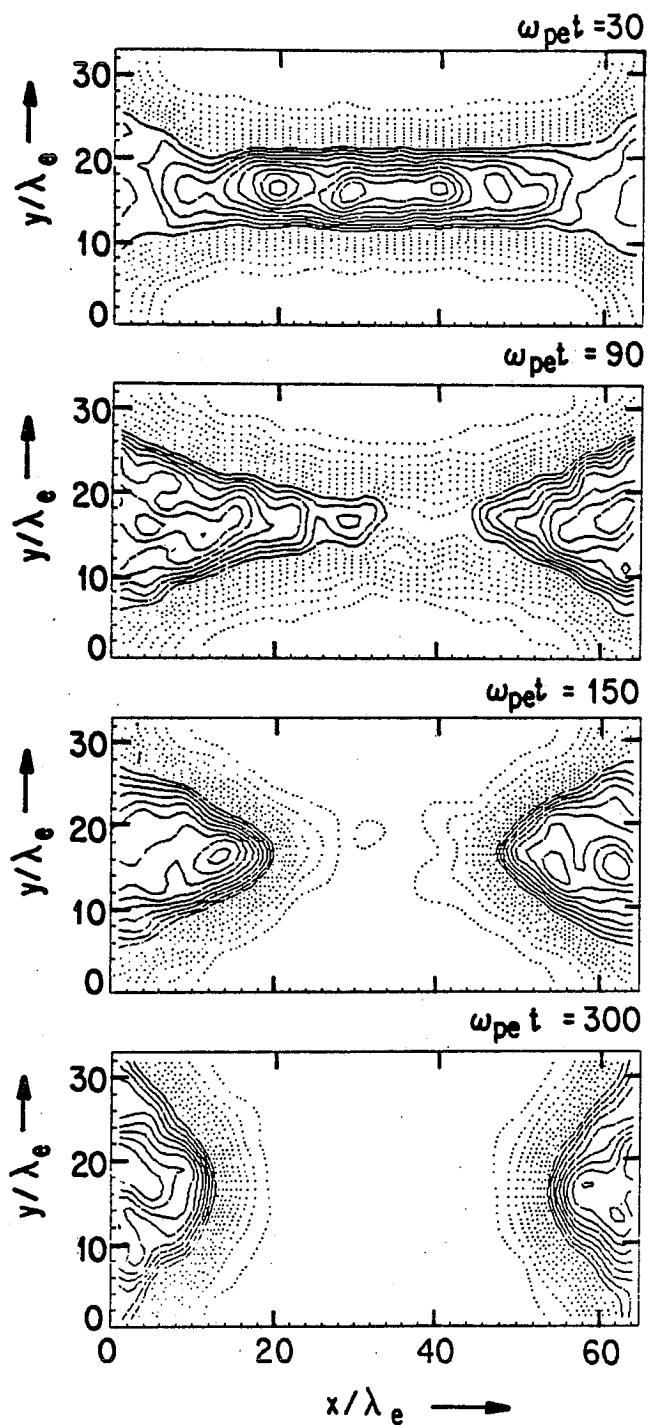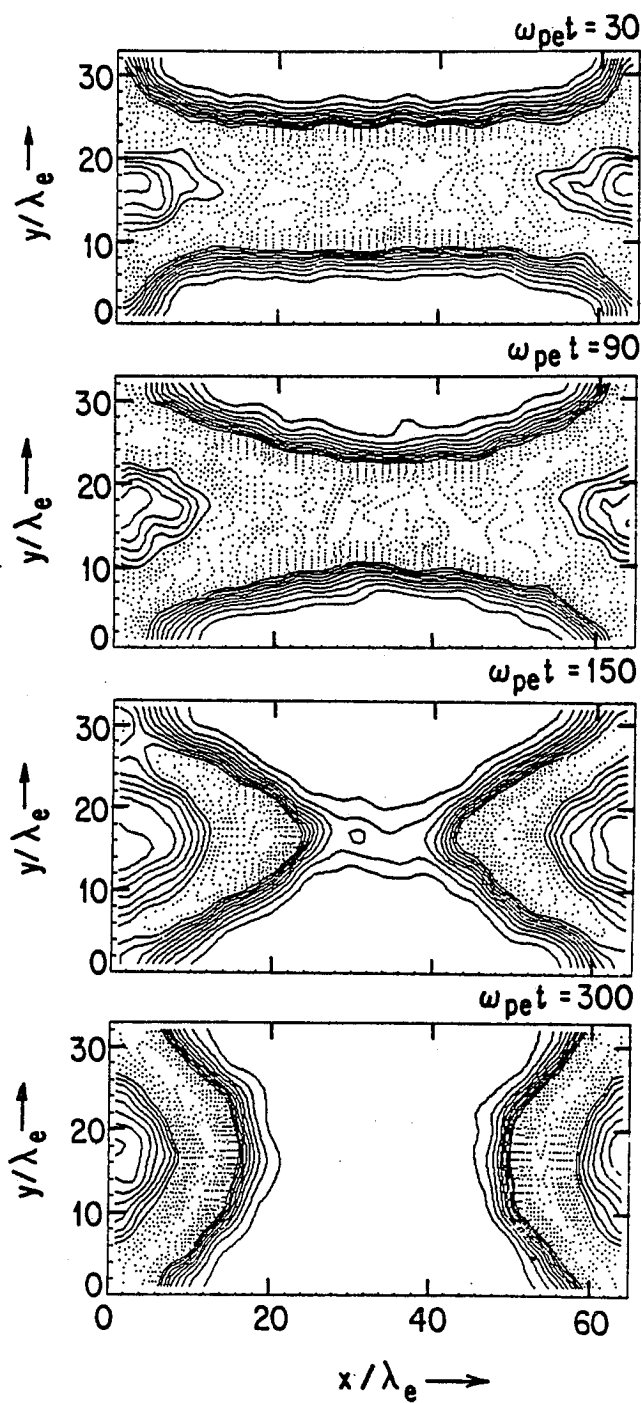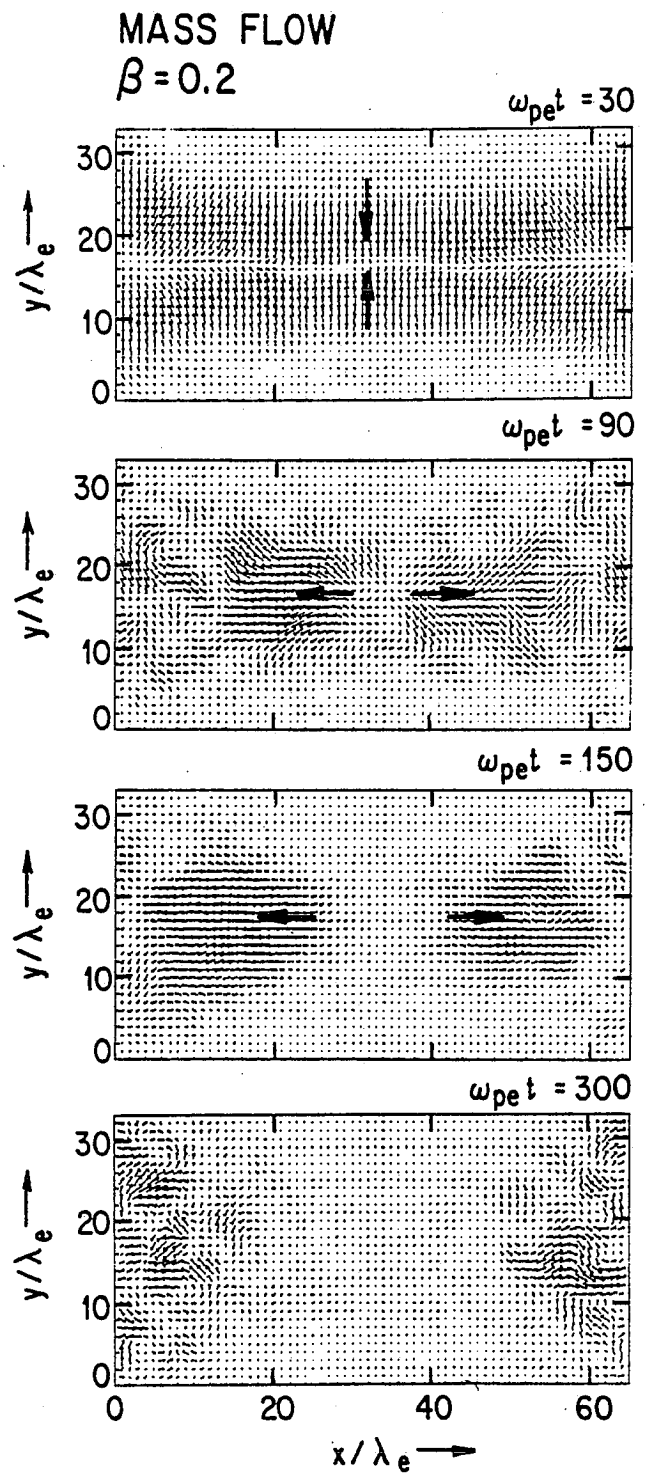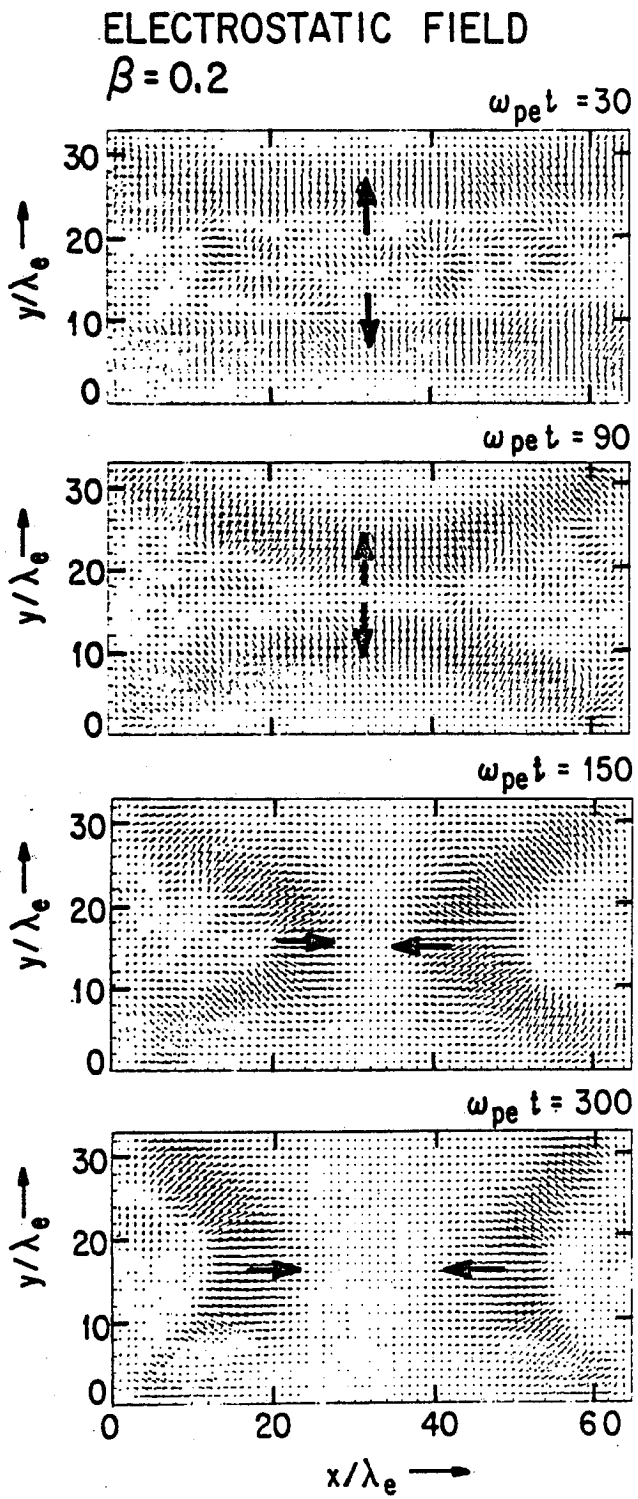
Figure 9

TEST PARTICLES ORBITS
$\beta = 0.2$

X - POINT ELECTRON
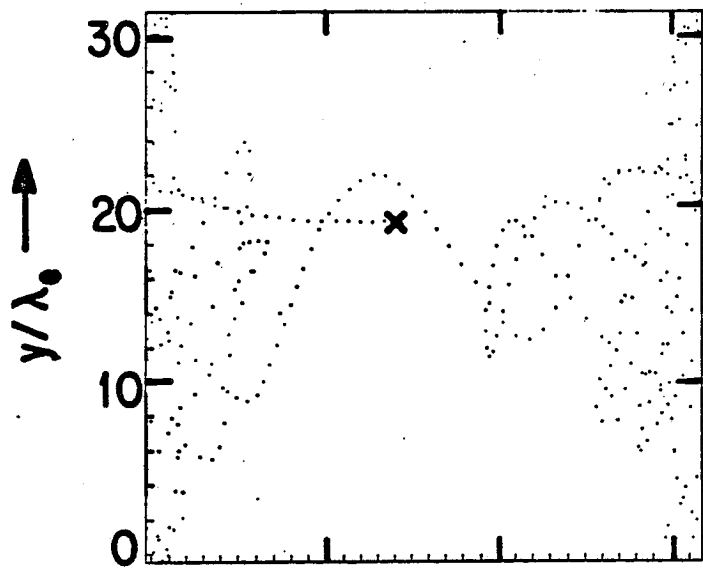
X - POINT ION
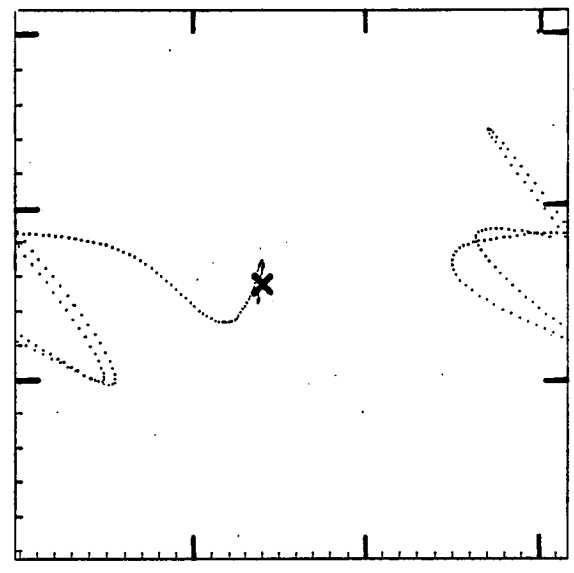
O - POINT ELECTRON
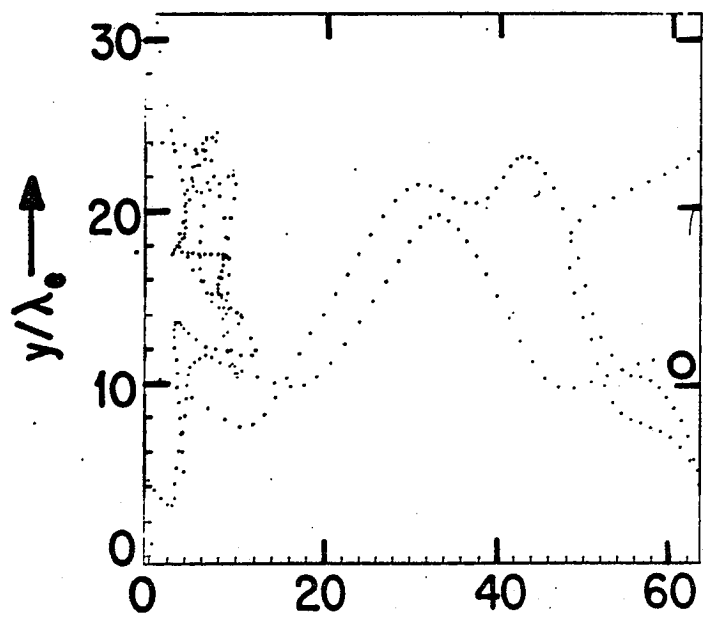
O - POINT ION
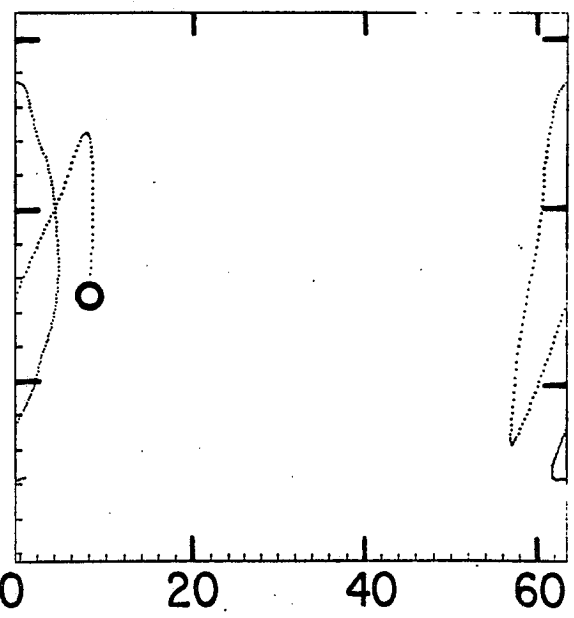
Figure 10

MAGNETIC FIELD LINES
$\beta = 0.2$

EXTERNAL FIELD
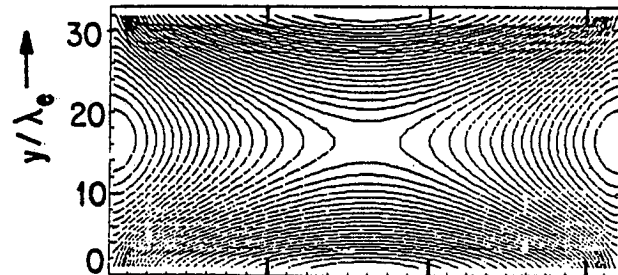
TOTAL FIELD $\omega_{pe}t = 50$
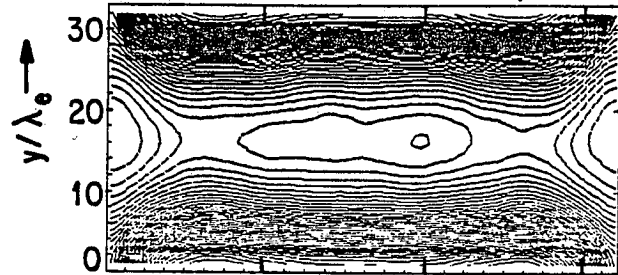
$\omega_{pe}t = 125$
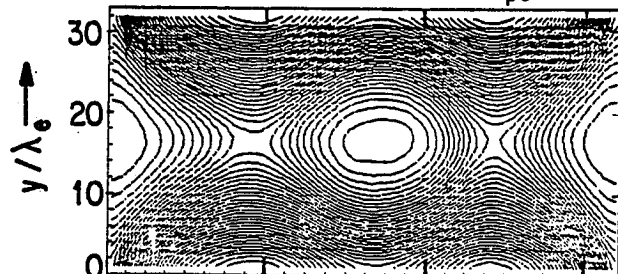
$\omega_{pe}t = 255$

$\omega_{pe}t = 375$

$x/\lambda_e \longrightarrow$

Figure 11

ION DENSITY
β =0.2
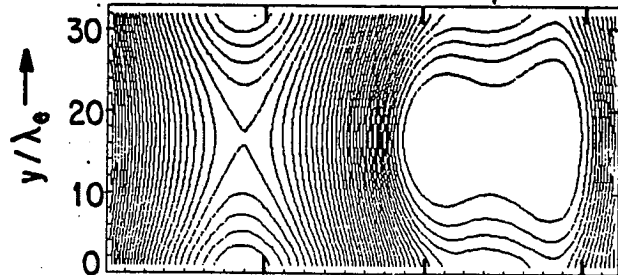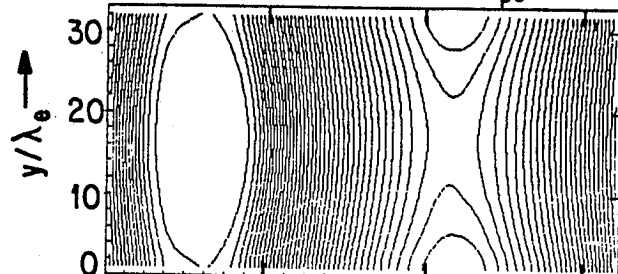
PLASMA CURRENT DENSITY
β=0.2
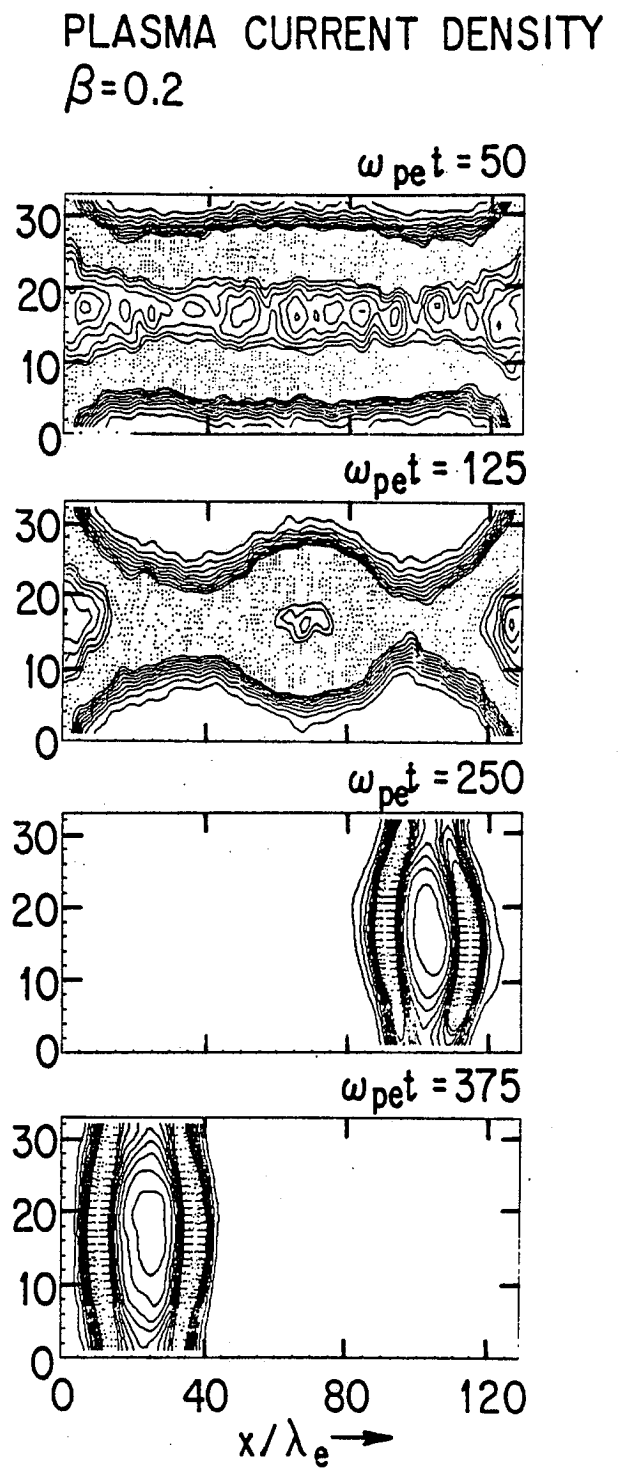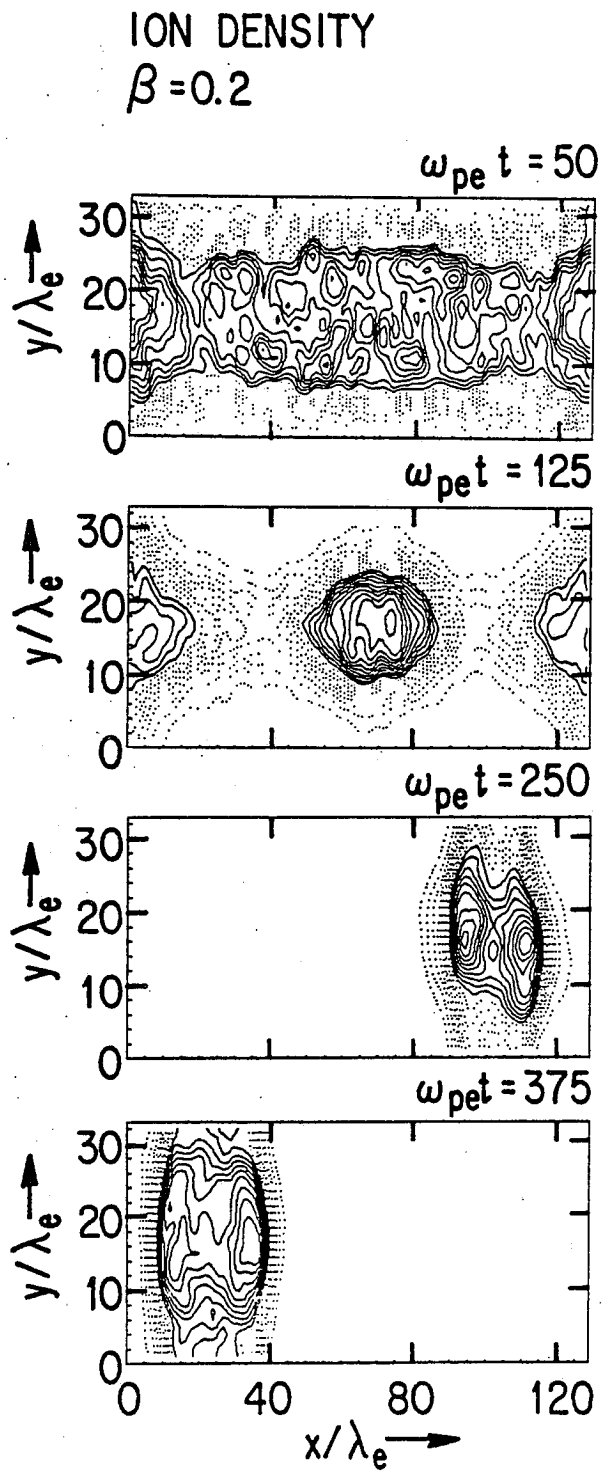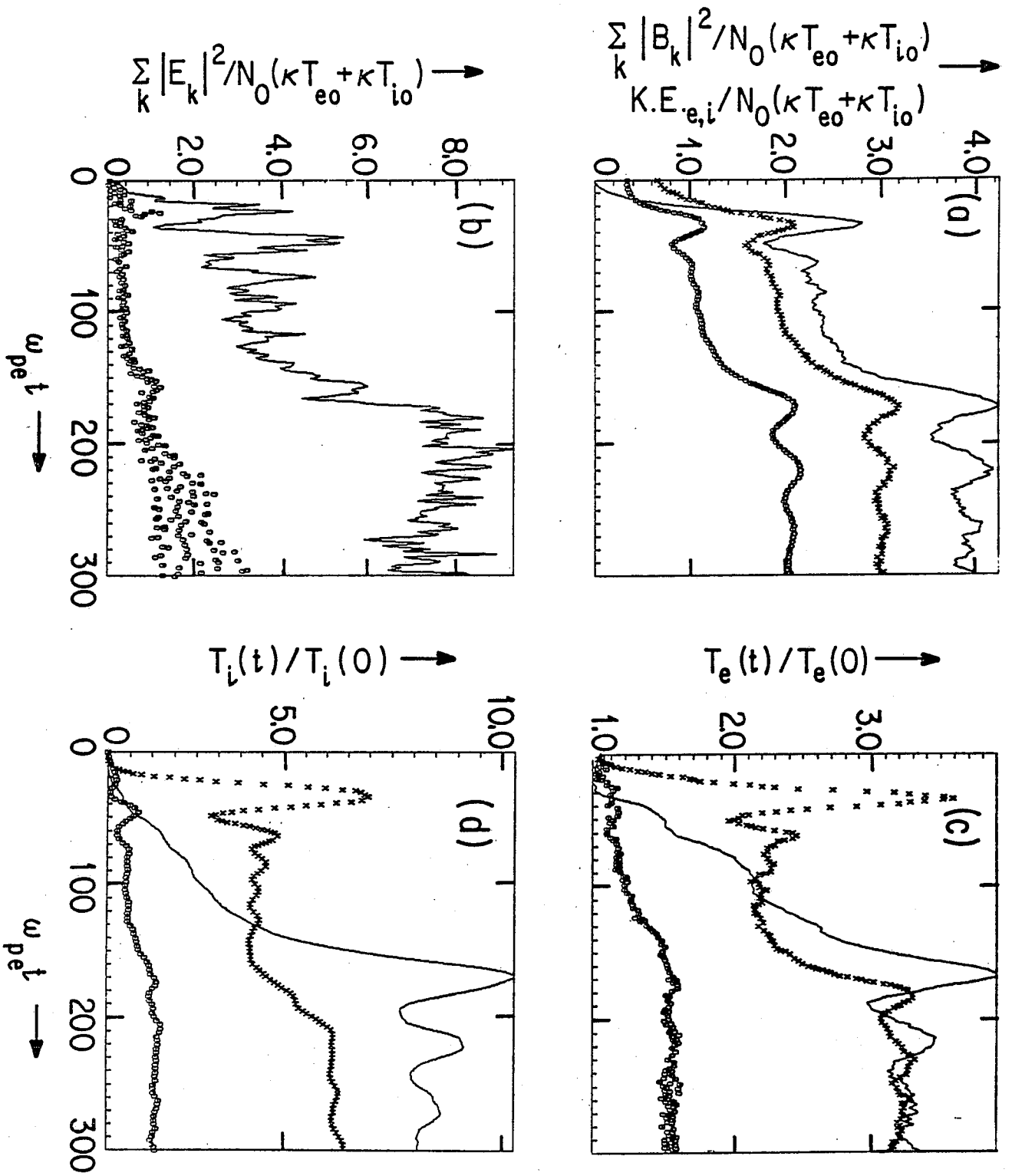

Figure 12

PLASMA CURRENT DENSITY
$\beta = 0.06$

Figure 13

Figure 14

$10^1 \frac{\Sigma}{k} |B_k|^2 / N_0 \kappa (T_{eo} + T_{io})$ →

$10^4 \frac{\Sigma}{k} |E_k|^2 / N_0 \kappa (T_{eo} + T_{io})$ → $10^1 K.E._{e,i} / N_0 \kappa (T_{eo} + T_{io})$

6.0

4.0

2.0

0

5.0
4.0
3.0
2.0
1.0
0

0   50   100   150   200

$\omega_{pe} t$ →

(a)

(b)

$T_i(t)/T_i(0)$ →

$T_e(t)/T_e(0)$ →

1.05
1.00
0.95

1.15
1.10
1.05
1.00

0   50   100   150   200

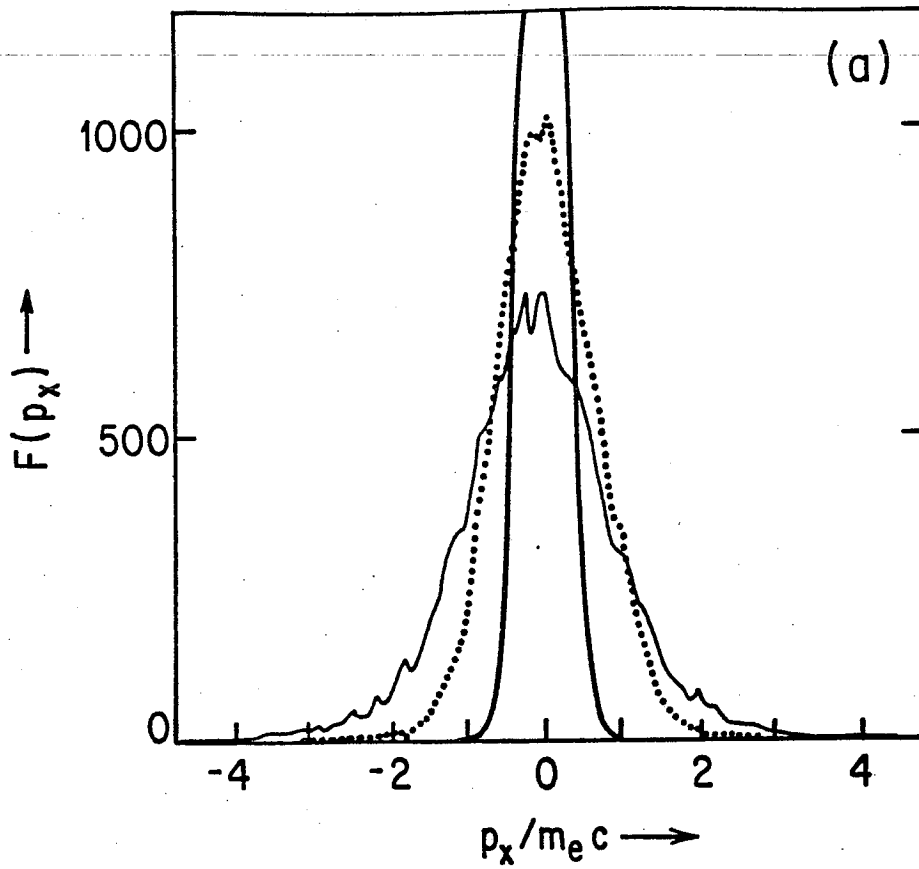$\omega_{pe} t$ →

(c)

(d)
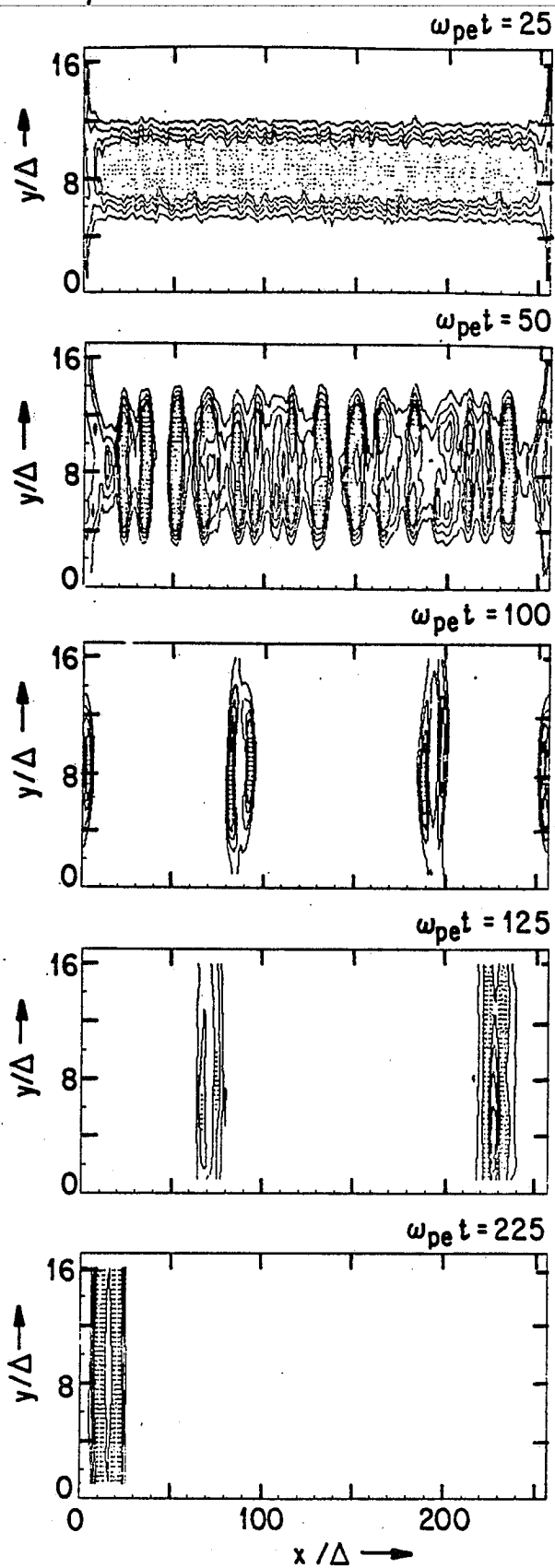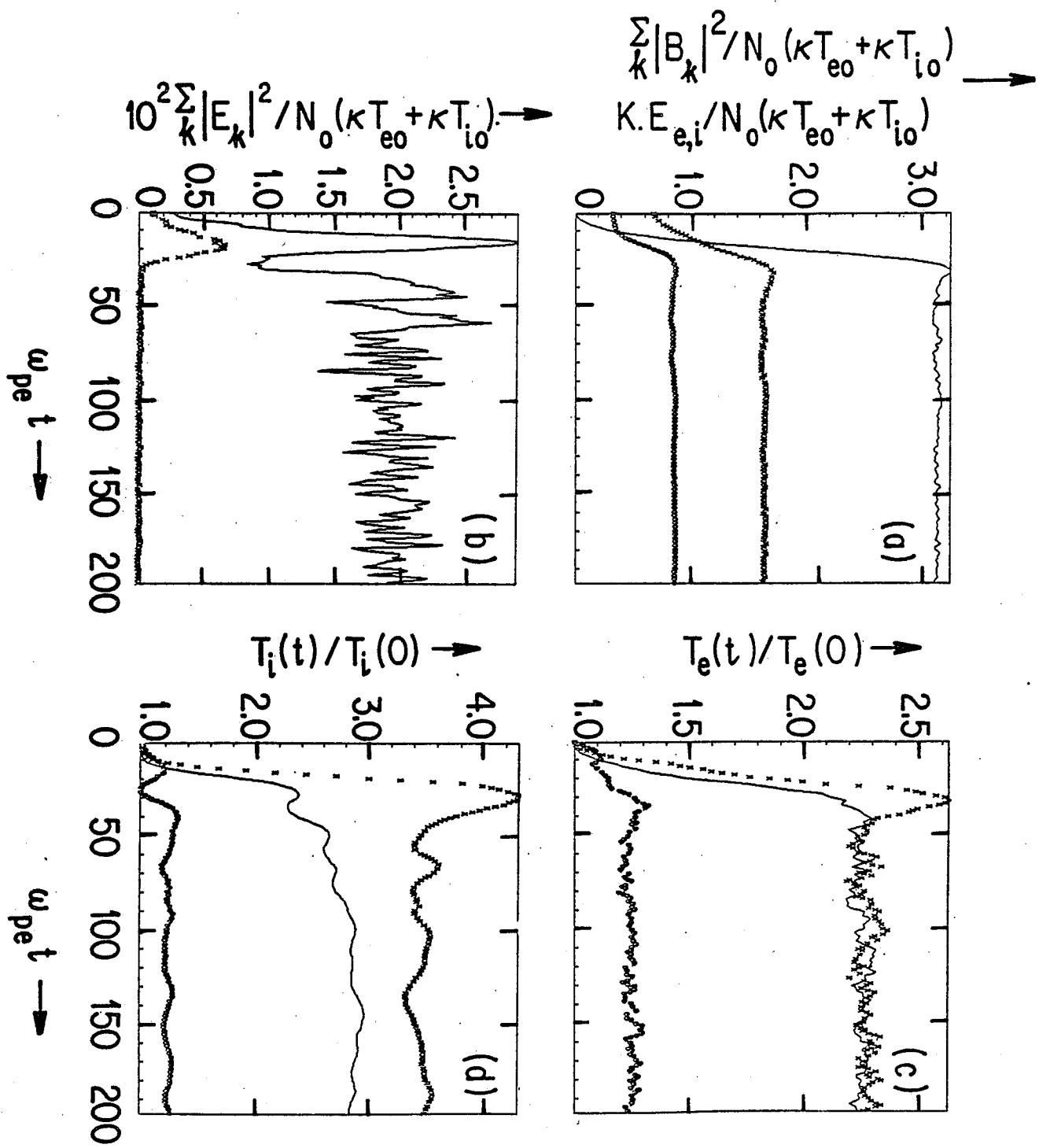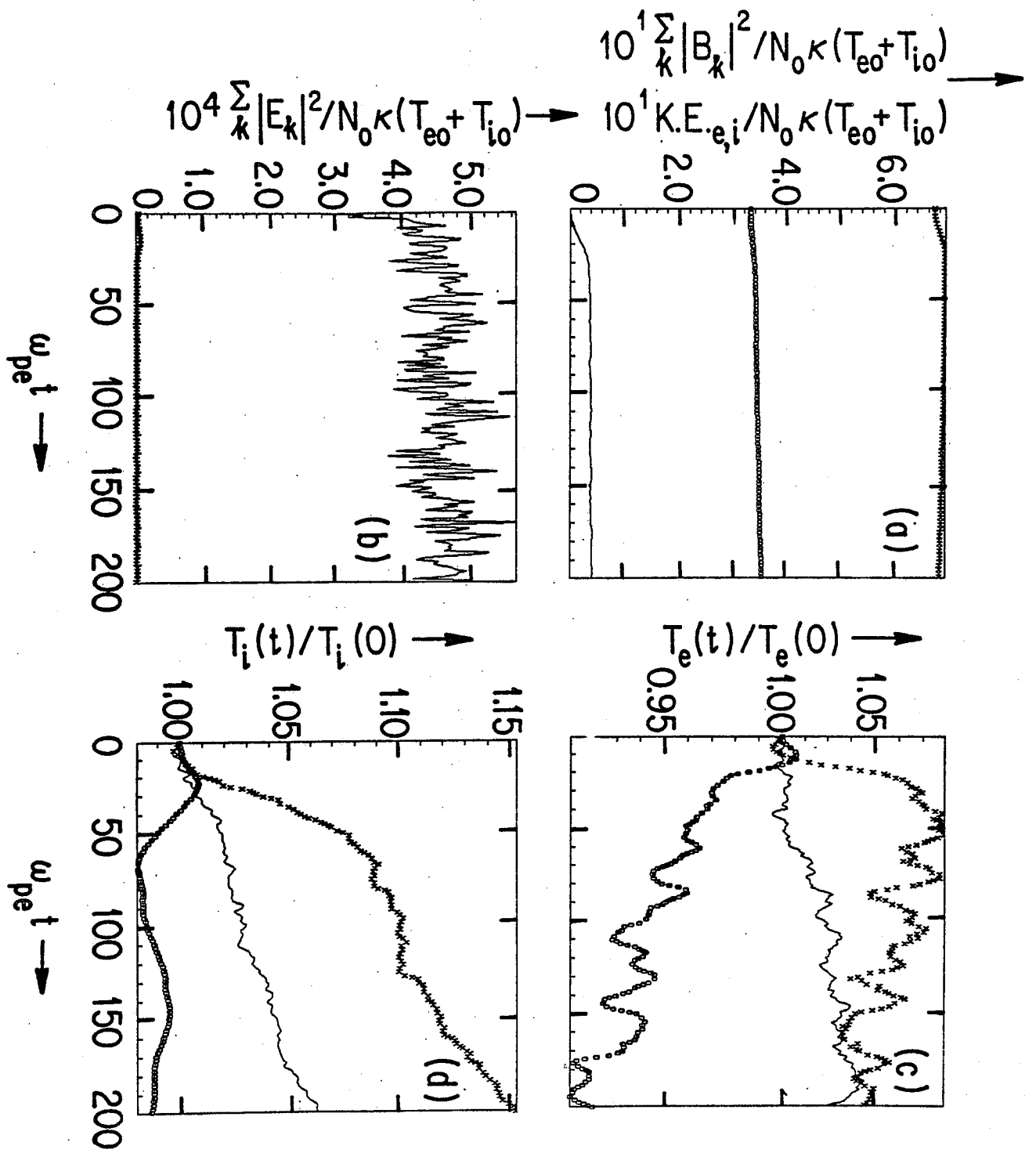
Figure 15

Figure 16

MODE (0, 1)

MODE (1, 0)

$\omega_{pe}t \longrightarrow$
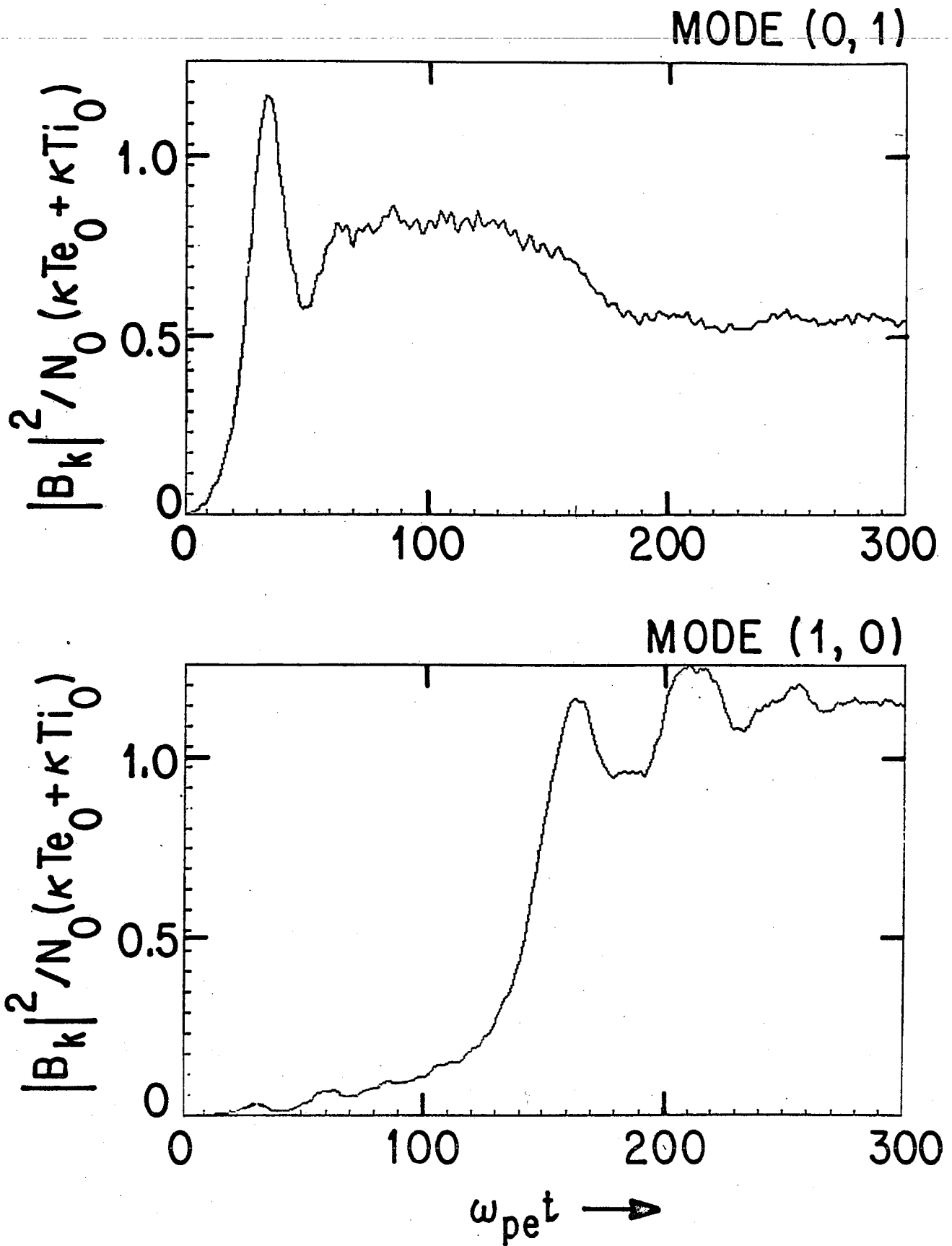
Figure 17

Figure 18

Figure 19

MODE (0, 1)

MODE (1, 0)

Figure 20

Figure 21